UNIVERSITY OF ÇUKUROVA
INSTITUTE OF NATURAL AND APPLIED SCIENCES

MSc THESIS

Mehmet VERGİLİ

JET ENERGY CALIBRATION STUDIES

DEPARTMENT OF PHYSICS

ADANA, 2006

UNIVERSITY OF CUKUROVA

THE INSTITUTE OF NATURAL AND APPLIED SCIENCES

JET ENERGY CALIBRATION STUDIES

By Mehmet VERGİLİ

MSc THESIS

DEPARTMENT OF PHYSICS

We certify that the thesis titled above was reviewed and approved for the award of degree of the Master by the board of jury on ..28.12.2006

İmza...	İmza...	İmza...
Assoc. Prof. İsa DUMANOĞLU	**Prof. Dr. Gülsen ÖNENGÜT**	**Assist. Prof. Sami ARICA**
Adviser	Member	Member

This Master Thesis is performed in Physics Department of the Institute of Natural and Applied Science of Cukurova University

Registration Number: 2967

T.C. ÇUKUROVA ÜNİVERSİTESİ FEN BİLİMLERİ ENSTİTÜSÜ MÜDÜRLÜĞÜ 1923

Prof Dr. Aziz ERTUNÇ
Director
The Institute of Natural and Applied Science

This Study was supported by Cukurova University Scientific Research Fund

Project Number: FBE.2006.YL.45

ABSTRACT

MSc THESIS

JET ENERGY CALIBRATION STUDIES

Mehmet VERGİLİ

DEPARTMENT OF PHYSICS
INSTITUTE OF NATURAL AND APPLIED SCIENCES
UNIVERSITY OF ÇUKUROVA

Supervisor: Assoc.Prof. İsa DUMANOĞLU
Year: 2006, Pages: 53
Jury: Assoc.Prof. İsa DUMANOĞLU
Prof. Gülsen ÖNENGÜT
Assist.Prof. Sami ARICA

We described dijet balancing, missing E_T projection fraction and photon-jet balancing to determine relative jet response as a function of pseudorapidity (η). We use CSA2006 data for missing E_T projection fraction and dijet balance method. For photon-jet balance method data was generated by us. All three methods were compared in this study. All analysis was based on reconstructed simulation data. These methods may be used for calibration or test of CMS calorimeter using simulated jet data. For determination of dijet balance, photon-jet balance and missing E_T projection fraction simulated QCD dijet data and photon-jet data was used in this study.

Key Words: dijet balance, missing transverse energy projection fraction, photon-jet balance, jet-met, calibration

ÖZ

MSc TEZİ

JET ENERJİ KALİBRASYON ÇALIŞMALARI

Mehmet VERGİLİ

ÇUKUROVA ÜNİVERSİTESİ
FEN BİLİMLERİ ENSTİTÜSÜ
FİZİK BÖLÜMÜ

Danışman: Doç.Dr. İsa DUMANOĞLU
Yıl: 2006, Sayfa: 53
Jüri: Doç.Dr. İsa DUMANOĞLU
Prof.Dr. Gülsen ÖNENGÜT
Yrd. Doç.Dr. Sami ARICA

η parametresine bağlı olarak göreli enerji düzeltmeleri iki jet enerji dengesi, kayıp dikine enerji iz düşüm kesri ve foton-jet enerji dengesi kullanılarak yapılabilir. Aynı yöntemler dedektörün η bağlı tepkisini belirlemek için de kullanılabilir. Bu çalışmada CMS'de simülasyon çalışmaları için üretilmiş CSA2006 QCD iki jet ve kendi ürettiğimiz foton-jet verileri kullanılmıştır. Ayrıca üç yöntemin birbirleri ile karşılaştırılması da yapılmıştır.

Anahtar Kelimeler: iki jet dengesi, kayıp dikine enerji izdüşüm kesri, foton-jet dengesi, jet-met, kalibrasyon

ACKNOWLEDGMENTS

I wish to thank my advisor, İsa DUMANOĞLU, for his encouragement and guidance during my master program. He always helped me about every subject.

I sincerely thank our group leader Gülsen ÖNENGÜT for her precious suggestions.

I would like to thank my friends Halil ÖZKURT, Cengiz ÖZBEK and, high energy group people at Cukurova University.

I thank the FNAL jetmet group members especially Robert HARRIS, Anwar BHATTI and Suichi KUNORI

Finally I thank my lovely fiancee Latife Nükhet ÖZBAYRAKTAR and my dear family for their love

CONTENTS **PAGE**

LIST OF TABLES **PAGE**

LIST OF FIGURES **PAGE**

ABBREVIATIONS

ADC	Analog Digital Converter
ALICE	A Large Ion Collider Experiment
ATLAS	A Toroidal LHC ApparatuS
CDF	Collider Detector at Fermilab
CERN	Conceil Europeenne pour la Recherche Nucleaire
CMS	Compact Muon Solenoid
DAQ	Data AcQusition
ECAL	Electromagnetic CALorimeter
HCAL	Hadron CALorimeter
LEP	Large Electron Positron Collider
LHC	Large Hadron Collider
LHC-b	Large Hadron Collider Beauty Experiment
QCD	Quantum ChromoDynamics
QED	Quantum ElectroDynamics
MPF	Missing ET Projection Fraction

1. INTRODUCTION

The Compact Muon Solenoid (CMS) is one of the four experiments at the Large Hadron Collider (LHC) at CERN. The LHC is scheduled to start running around 2007. CMS physics goals include the search for the theoretical Higgs boson, supersymmetric (SUSY) particles, new massive vector bosons, extra dimensions, Standard Model, heavy-ion physics.

Jets are defined as localised energy depositions in the calorimeters and are reconstructed using an iterative clustering algorithm with a fixed cone of radius in η, ϕ space. Jets are ordered in transverse energy, where E is the scalar sum of energy deposited in the calorimeter towers within the cone, and θ is the angle formed by the beam-line, the event vertex, and the cone centre.

The missing transverse energy is defined as the negative vector sum of the transverse energy in the electromagnetic and hadronic calorimeter towers, $E_T^{miss} = -\sum(E_i \sin\theta_i)\hat{n}_i$ where E_i is the energy of the i-th tower, $\hat{n}_i$ is a transverse unit vector pointing to the centre of each tower, and θ_i is the polar angle of the tower; the sum extends to $\eta < 5$.

The huge QCD cross section ensures that jets will dominate high-P_T physics at the LHC. Jets will not only provide a benchmark for understanding the detector, but will also serve as an important tool in the search for physics beyond the standard model. Event signatures for SUSY, Higgs boson production, compositeness, and other new physics processes require accurate reconstruction and measurement of jets coming from high-P_T quarks and gluons. The problems with associating a jet measured in a calorimeter with a scattered parton is an old, persistent problem in hadron collisions. Jet energy resolution and linearity are key factors in separating signal events from backgrounds. Missing transverse energy resolution, which historically has played an important role in the discoveries of the W boson and the top quark and the search for new phenomena at hadron colliders, is closely related to the calorimeter jet energy response.

There are different jet clustering algorithms used in literature. In this study midpoint cone algorithm will be used. and we describe how these jets are then corrected to correspond to the energy of the parent parton. Briefly the generic jet energy corrections include;

- Relative energy corrections which correct jets back to an equivalent jet in the η

range of $0 < |\eta| < 5,2$ to make the calorimeter responsee uniform in η

• Multiple pp interaction corrections which subtract the energy due to additional pp interactions from the jet energy

• Absolute jet energy corrections which convert the calorimeter cluster p_T to the $\sum p_T$ of particles in the cone (calorimeter energy to particle energy)

• Underlying event corrections which subtract the energy due to underlying event (fragmentation of partons which are not associated with the hard scattering) from the jet energy.

• Out-of-cone corrections which accounts for the energy that leaks outside the jet cone due to fragmentation effects and soft gluon radiation.

This thesis presents study of relative jet energy corrections which correct jets for any variation with detector η.

In this thesis relative jet energy correction is including 3 different methods. These are;

Dijet Balance method (B_{PT})

Missing E_T Projection Fraction method (MPF)

Photonjet Balance method (B_γ)

Dijet balancing can be used to measure relative jet response and resolution from real jet data. In dijet balance one jet is required to be in the barrel. The other jet is called the probe jet. Conservation of momentum for a $2 \rightarrow 2$ process requires they have the same P_T. The mean of the P_T difference between the two jets measures the response difference between the probe region and the barrel. The RMS of the P_T difference measures the jet resolution.

Missing ET Projection Fraction (MPF) has been claimed as another method for calculating relative energy corrections and is less dependent on how well the third jet is clustered and results in a beter dijet balancing resolution.

In Photon-jet balancing we used photon p_T and probe jet p_T in order to determine photon-jet balancing correction method.

In this thesis the dijet balance, MPF and photon-jet balance methods are compared for the simulated CMS data.

2. PHYSICS AND CMS DETECTOR REQUIREMENTS

2.1 Search for the Higgs Boson

In the design phase of CMS and ATLAS in the early 1990s, the detection of the SM Higgs boson was used as a benchmark to test the performance of the proposed designs. It is a particularly appropriate benchmark since there is a wide range of decay modes depending on the mass of the Higgs boson. The current lower limit on the mass of the Higgs boson from LEP is 114.4 GeV/c^2. In the vicinity of this limit, the branching fractions of the Higgs boson are dominated by hadronic decays, which are difficult to use to discover the Higgs boson at the LHC due to the large QCD backgrounds and the relatively poor mass resolution that is obtainable with jets. Hence, the search is preferentially conducted using final states that contain isolated leptons and photons, despite the smaller branching ratios.

The natural width of the Higgs boson in the intermediate-mass region (114 $GeV/c^2 < m_H < 2m_Z$) is only a few MeV, and the observed width of a potential signal will be dominated by the instrumental mass resolution. In the mass interval 114 130 GeV/c^2, the two-photon decay is one of the principal channels likely to yield a significant signal. Central exclusive production of the Higgs might offer the only way to access the $b\bar{b}$ decay mode. The Higgs boson should be detectable via its decay into two Z bosons if its mass is larger than about 130 GeV/c^2 (one of the Zs is virtual when m_H is below the ZZ threshold). For $2m_Z < m_H < 600$ GeV/c^2 the ZZ decay, with its four-lepton final states, is the mode of choice.

In the region 600 ¡ m_H ¡ 1000 GeV/c^2, the cross section decreases so that higher branching fraction modes involving jets or E_T^{miss} from W or Z decays have to be used. The jets from W and Z decays will be boosted and may be close to each other in η, ϕ space.

The dominant Higgs-boson production mechanism, for masses up to about 700 GeV/c^2, is gluon-gluon fusion via a t-quark loop. The WW or ZZ fusion mechanism becomes important for the production of higher-mass Higgs bosons. Here, the quarks that emit the Ws or Zs have transverse momenta of the order of W and Z masses. The detection of the resulting high-energy jets in the forward regions ($2 < |\eta| < 5$) can be used to tag the reaction, improving the signal-to-noise ratio and extending the range of masses over which the Higgs can be discovered. These jets are highly boosted and their transverse size is similar to that of a high-energy hadron shower.

2.2 Search for Supersymmetric Particles

The decays of supersymmetric particles, such as squarks and gluinos, involve cascades that, if R-parity is conserved, always contain the lightest SUSY particle (LSP). The latter is expected to interact very weakly, thus leading to significant E_T^{miss} in the final state. The rest of the cascade results in an abundance of leptons and jets (particularly b-jets and/or τ -jets). In GMSB schemes with the LSP decaying into a photon and gravitino, an increased number of hard isolated photons is expected.

2.3 Search for New Massive Vector Bosons

The detector requirements for high momenta can be determined by considering decays of high-mass objects such as $Z' \rightarrow e^+e^-$ and $\mu^+\mu^-$. The discovery of an object like a Z' boson will, very likely, be limited by the statistical significance of the signal. Ways of distinguishing between different models involve the measurement of the natural width and the forward backward asymmetry, both of which require sufficiently good momentum resolution at high $p_T(\triangle pT/pT < 0.1$ at $p_T \approx 1TeV/c)$ to determine the sign of the leptons and a pseudorapidity coverage up to $\eta = 2.4$.

2.4 Extra Dimensions

The existence of extra dimensions can lead to a characteristic energy scale of quantum gravity, M_D, which is the analogue of the Planck mass in a D-dimensional theory, and which could lie just beyond the electroweak scale. In terms of experimental signatures, 3 regimes can be distinguished: i) Cis-Planckian, where $E \ll M_D$, leading to signals involving the emission of gravitons that escape into extra dimensions, e.g. $pp \rightarrow jet + graviton \rightarrow jet + E_T^{miss}$, ii) Planckian, $E \approx M_D$, leading to model-dependent signatures. In string-theory motivated models there are Regge-like excitations that manifest themselves as Z-like resonances with $\approx$ TeV separations in mass, iii) Trans-Planckian, $E \gg M_D$, leading to anomalous high mass dijet production and to mini black hole production with spectacular decays involving equal and democratic production of fundamental particles such as leptons, photons, neutrinos, W, Z, jets, etc. The resulting production and kinematic distributions could allow the determination of the Hawking temperature, the mass of the black holes, the number of extra dimensions, etc.

2.5 Standard Model

The LHC will also allow studies of QCD, electroweak, and flavour physics. Precision studies can give indications for physics beyond the SM, providing complementary information with respect to direct searches. As an example, extensive tests of QCD will be possible through the measurement of the production of jets and direct photons with transverse energies up to 34 TeV and from cross-section measurements which fall by 11 orders of magnitude. Top quarks will be produced at the LHC with a rate measured in Hz, thus the opportunity to test the SM couplings and spin of the top quark is available provided good identification of b-jets in the decays is possible. Searches for flavour changing neutral currents, lepton flavour violation through $\tau \longrightarrow 3\mu$ or $\tau \longrightarrow \mu\gamma$, measurements of $B_s^o \longrightarrow \mu\mu$, measurements of triple and quartic gauge couplings, etc. can open a window onto new physics. Finally, in association with TOTEM, CMS will be able to cover the full range of diffractive physics as well.

2.6 Heavy-ion Physics

The recent results from RHIC indicate that very strongly interacting nuclear matter is produced in high energy heavy-ion collisions. The most striking experimental signatures of the produced matter are the suppression of high p_T particles (jet quenching) and the strong elliptical flow approaching the hydrodynamic limit. The increase in collision energy from $\sqrt{NN} = 200\ GeV/c^2$ at RHIC to 5500 GeV/c^2 at LHC will allow the extension of studies of jet quenching to much higher p_T and the identification of fully formed jets. The measurements of energy flow at LHC will stringently test the liquid-like behavior of the hot nuclear matter. The increased energy will also allow studies of presently inaccessible hard probes like Υ and Z^0. The studies of jet quenching, energy flow, and quarkonium production will require large-acceptance, high-resolution calorimeters and tracking devices, as well as a flexible trigger.

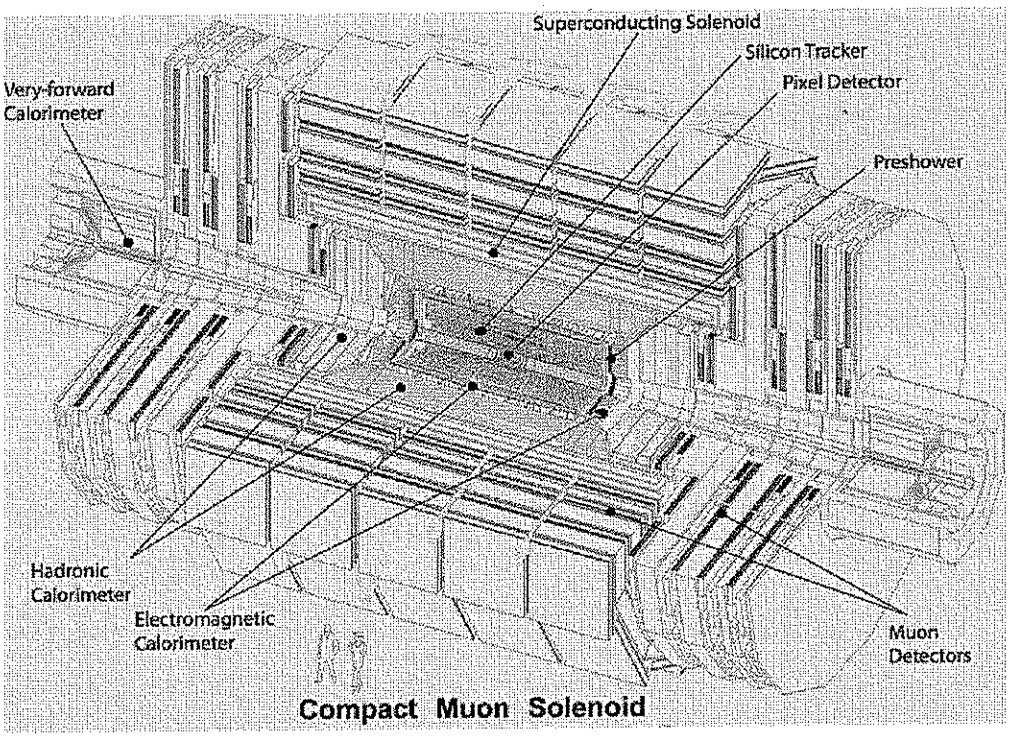

Figure 3.1 A schematic view of the CMS detector.

divided into the TEC (Tracker End Cap) and TID (Tracker Inner Disk). Each TEC comprises 9 disks that extend into the region 120 cm $< |z| <$ 280 cm, and each TID comprises 3 small disks that fill the gap between the TIB and the TEC

Pixel Tracker: The pixel detector consists of 3 barrel layers with 2 endcap disks on each side of them. The 3 barrel layers are located at mean radii of 4.4 cm, 7.3 cm and 10.2 cm, and have a length of 53 cm. The 2 end disk, extending from 6 to 15 cm in radius, are placed on each side at $|z| =$ 34.5 cm and 46.5 cm.

3.2 Calorimeters

The CMS calorimeter has 2 two parts: electromagnetic calorimeter and hadronic calorimeter and these calorimeters is divided into central, endcap and forward section.

3.2.1 Electromagnetic Calorimeter

The Electromagnetic Calorimeter (ECAL)is a hermetic, homogeneous calorimeter comprising 61200 lead tungstate ($PbWO_4$) crystals mounted in the central barrel part, closed by 7324 crystals in each of the 2 endcaps .

The Barrel section (EB) has an inner radius of 129 cm. It is structured as 36 identical "supermodules" each covering half the barrel length and corresponding to a pseudorapidity interval of $0 < |\eta| < 1.479$. The crystals are quasi-projective (the axes are tilted at 3^o with respect to the line from the nominal vertex position) and cover 0.0174 (i.e. 1^o) in $\triangle\phi$ and $\triangle\eta$.

The endcaps (EE), at a distance of 314 cm from the interaction vertex and covering a pseudorapidity range of $1.479 < |\eta| < 3.0$, are each structured as 2 "Dees", consisting of semi-circular aluminium plates from which are cantilevered structural units of 5×5 crystals, known as "supercrystal".

3.2.2 Hadronic Calorimeter

The design of the hadron calorimeter (HCAL) is strongly influenced by the choice of magnet parameters since most of the CMS calorimetry is located inside the magnet coil and surrounds the ECAL system. An important requirement of HCAL is to minimize the non-Gaussian tails in the energy resolution and to provide good containment and hermeticity for the E_T^{miss} measurement. Hence, the HCAL design maximizes material inside the magnet coil in terms of interaction lengths. This is complemented by an additional layer of scintillators, referred to as the hadron outer (HO) detector, lining the outside of the coil.

The Hadron Barrel (HB) part of HCAL consist of 32 towers covering the pseudorapidity region $-1.4 < \eta < 1.4$, resulting in 2304 towers with a segmentation $\triangle\eta \times \triangle\phi = 0.087 \times 0.087$. The HB is constructed in 2 half barrels.

The Hadron Outer (HO) detector contains scintilators with a thickness of 10 mm, which line the outside of the outer vacuum tank of the coil and cover the region $-1.26 < \eta < 1.26$. The tiles are grouped in 30^o sectors, matching the ϕ segmentation of the drift tube chambers. They sample the energy from penetrating hadron showers leaking through the rear of the calorimeters and so serve as a "tail-catcher" after the magnet coil.They increase the effective thickness of the hadron calorimeter to over 10 interaction lengths, thus reducing the tails in the energy resolution function. The HO also improves the E_T^{miss} resolution of calorimeter.

The Hadron Endcap (HE) consists of 13 η towers with 5^o ϕ segmentation, covering the pseudorapidity region $1.3 < |\eta| < 3.0$. For the 5 outermost towers (at smaller η) the ϕ segmentation is 5^o and the η segmentation is 0.087. For the 8 high η the ϕ segmentation is 10^o, whilst the η segmentation varies from 0.09 to 0.35 at the highest η. The total number of HE towers is 2304.

The Hadron Forward (HF) covers the region $3.0 < |\eta| < 5.19$ and it has 13 towers in η. All towers size are given by $\Delta\eta \approx 0.175$, except for the lowest-η tower with $\Delta\eta \approx 0.1$ and the highest-η tower with $\Delta\eta \approx 0.3$. The ϕ segmentation of all towers is 10^o, except for the highest-η one which has $\Delta\phi = 20^o$. This leads to 900 towers and 1800 channels in the 2 HF modules.

If we calculate the hadron calorimeter η rings we will find 84 according to above introduction. However Hadron calorimeter is divided 82 η region because HE and HB overlap in the region $1.305 < |\eta| < 1.392$.

4. JET CLUSTERING ALGORITHMS

Jet is a group of particle which is defined in different ways. In the calorimeter we calculate a jet energy from the energy deposited in the calorimeter towers using a jet clustering algorithm. For this study, jets are clustered using midpoint cone algorithm with a fixed cone size in which the center of the jet is defined as (η^{jet}, ϕ^{jet}) and the size of the jet cone as $R = \sqrt{(\eta^{tower} - \eta^{jet})^2 + (\phi^{tower} - \phi^{jet})^2} = 0.5$. The jet corrections and uncertainties are estimated for this cone size.

In Monte Carlo (MC) simulation, particle jets are obtained using the same jet clustering algorithm on stable state particles.

The towers are used as input to several jet clustering algorithms. The energy associated with a tower is calculated as the sum of all contributing readout cells which pass the online zero suppression threshold and any additional offline software thresholds. For the purpose of jet clustering, the towers are treated as massless particles, with the energy given by the tower energy, and the direction defined by the interaction point and the center of the tower.

4.1 Iterative Cone Algorithm

The algorithm starts with the highest E_T of calorimeter tower (or particles to find generator level jets) from the sorted calorimeter towers (in decreasing order) in which the E_T of the towers are above the specified seed threshold. The distance R in (η, ϕ) space between the first object and the other objects in the list is calculated and the objects inside the cone $R < R^C$ (where R^C is the size of the cone in the algorithm) are used to obtain proto-jets. Proto-jet transverse energy and direction is defined by using the objects inside the cone as

$$E_T = \sum_i E_T^i \tag{4.1}$$

$$\eta = \frac{1}{E_T} \sum_j \eta_j E_T^j \tag{4.2}$$

$$\phi = \frac{1}{E_T}\sum_j \phi_j E_T^j \tag{4.3}$$

The computed direction is used to seed a new proto-jet. The procedure is repeated until the following conditions are satisfied

$$E_T^{n+1} - E_T^n < 1\% \tag{4.4}$$

$$\sqrt{(\triangle\eta)^2 + (\triangle\phi)^2} < 0.01 \tag{4.5}$$

When a stable proto-jet is found, all objects in the proto-jet are removed from the list of input objects and the stable proto-jet is added to the list of jets. The whole procedure is repeated until the list contains no more objects with an E_T above the seed threshold. The cone size R^C and the seed threshold are parameters of the algorithm.

4.2 Midpoint Cone Algorithm

The midpont-cone algorithm was designed to facilitate the splitting and merging of jets. The midpoint-cone algorithm also uses an iterative procedure to find stable cones (proto-jets) starting from the cones around objects with an E_T above a seed threshold. In contrast to the iterative cone algorithm described above, no object is removed from the input list. This can result in overlapping proto-jets (a single input object may belong to several proto-jets). To ensure the collinear and infrared safety of the algorithm, a second iteration of the list of stable jets is done. For every pair of proto-jets that are closer than the cone diameter, a midpoint is calculated as the direction of the combined momentum. These midpoints are then used as additional seeds to find more proto-jets. When all proto-jets are found, the splitting and merging procedure is applied, starting with the highest E_T proto-jet. If the proto-jet does not share objects with other proto-jets, it is defined as a jet and removed from the proto-jet list. Otherwise, the transverse energy of the proto jet pair are compared. If the fraction is greater than f (typically 50%) the proto-jets are merged, otherwise the shared objects are individually assigned to the proto-jet that is closest in η, ϕ space. The procedure is repeated, again always starting with the highest E_T proto-jet, until no proto-jets are left. This algorithm implements the energy scheme to calculate the proto-jet properties but a different recombination scheme may be used for the final jet. The parameters of the algorithm include a seed threshold, a cone radius, a threshold f on the shared energy fraction for jet merging, and also a maximum number of proto jets that are used to calculate midpoints.

5. DATA SET

In this study all of data samples are produced by CMSSW simulation packages program. We used QCD events from CSA06 for Dijet Balance and Missing E_T Projection fraction.

In CSA2006 data we found a problem. Particles with $p > 1$ TeV has been not simulated correctly. There was sudden increase at 1 TeV. But this problem does not effect our study because we used properly seperated energy bins.

For photon jet balance we used photon-jet data. These data was produced by us. For production we used CMSSW-090 version with 4 step, generation with pythia, simulation, digitization and reconstraction.

As can be seen from Table-5.1 CSA06 data has different p_T from 80 GeV to 14000 GeV. And also photon-jet data is shown in Table-5.2.

Table 5.1 QCD Skims of the CSA06 Jet Soup in the following range of p_T hat in GeV (hard collision transverse momemtum).

Sample p_T Range (GeV)	Number of Event
80-120	45991
120-170	45255
170-230	45014
230-300	44995
300-380	45274
380-470	44009
470-600	44778
600-800	27311
800-1000	26633
1000-1400	26647
1400-1800	26640
1800-2200	26536
2200-2600	26214
2600-3000	26356
3000-3500	26859
3500-14000	25912

Table 5.2 Gamma Jet Data range of p_T hat in GeV.

Sample p_T Range (GeV)	Number of Event
80-120	6000
120-170	6000
170-230	6000

6. RELATIVE ENERGY CORRECTIONS

6.1 Correction Using Dijet Balancing Method

In dijet balancing the two jets with highest p_T in the event (the leading jets) are found and events are selected by requiring at least one leading jet to have $|\eta| < 1$ (the barrel jet). To measure jet response versus η the other leading jet (the probe jet) may have any η value. If both leading jets have $|\eta| < 1$ the one that is designated as probe jet is chosen randomly so that each jet has equal chance of being the probe. Avarege p_T for dijet is defined by

$$p_T^{ave} = \frac{p_T^{probe} + p_T^{barel}}{2} \tag{6.1}$$

We selected the dijet p_T range in the calorimeter as the avarage p_T of two leading jet. See Fig.6.1.

For calculation of the dijet balance, the data was divided η of the calorimeter and the distribution of the dijet balance was determined

$$B_{PT} = \frac{p_T^{probe} - p_T^{barrel}}{p_T^{ave}} \tag{6.2}$$

In Fig.6.2 dijet balance is shown for $80 < p_T^{ave} < 120$ GeV and for different η regions which cover the whole range of the CMS calorimeter. For jets with high p_T, $0 < |\eta| < 1$ region (central region) has more event than other eta regions. But as can be seen $2.0 < \eta < 3.5$ region (endcap region) has many event because of low p_T. The jets with very high p_T doesn't reach $|\eta| > 1$ region.

During this study several cuts are placed to reduce the effects of gluon radiation:

• The jets are required to be back to back in the $r - \phi$ plane, i.e. the difference of their azimuthal angle, $\triangle\phi(jet_{probe}, jet_{barrel})$, should be larger then 2.7 radians.

• If a 3rd jet is present in the event, the p_T of this 3rd jet should be less than 8 GeV.

We did not use here these cut because of not having enough statistics.

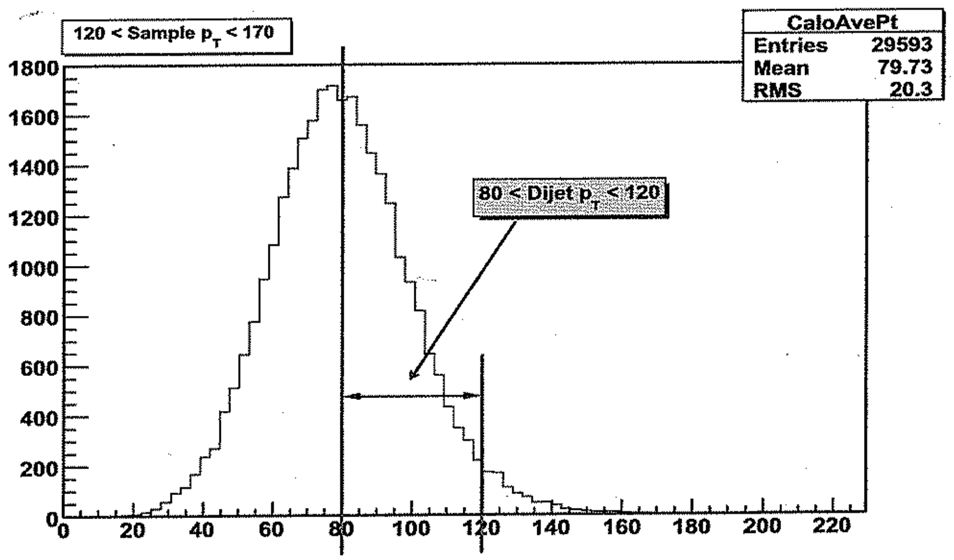

Figure 6.1 Avarage p_T of two leading Calorimeter jet. As can be seen from the figure the dijet p_T range is different than the p_T range of the sample.

6.1.1 Response Measurement

The relative response defined as the fractional difference between the jet response in the probe region and the jet response for $|\eta| < 1$, is then

$$R_{B_{PT}} = \frac{2 + \langle B_{PT} \rangle}{2 - \langle B_{PT} \rangle} = \frac{p_T^{probe}}{p_T^{barrel}} \tag{6.3}$$

where $\langle B_{PT} \rangle$ is mean value of the dijet balance distribution. Note, that $R_{B_{PT}}$ is mathematically equal to p_T^{probe}/p_T^{barrel}. However, by inferring $R_{B_{PT}}$ from B_{PT} we reduce the sensitivity of our measurement to non-Gaussian tails since the B_{PT} distribution is in good approximation a Gaussian distribution unlike the distribution of p_T^{probe}/p_T^{barrel}.

In CMS calorimeter we have 82 towers which have different η sizes and cover the whole detector. We separeted the CMS calorimeter using these η ranges. And then for response determination we calculated the mean of dijet balance distribution for each of 82 towers. In fig.6.3 dijet balance distribution is shown for tower 16. We have 82 dijet balance distributions similarly.

In Fig.6.4, we show a simulation of the measurement of response from dijet balancing (B_{PT}) versus η for a cone size of jet 0.5 and for transverse momentum region $80 < p_T^{ave} <$ 120 GeV. In Fig.6.5, we show the response for larger values of dijet p_T.

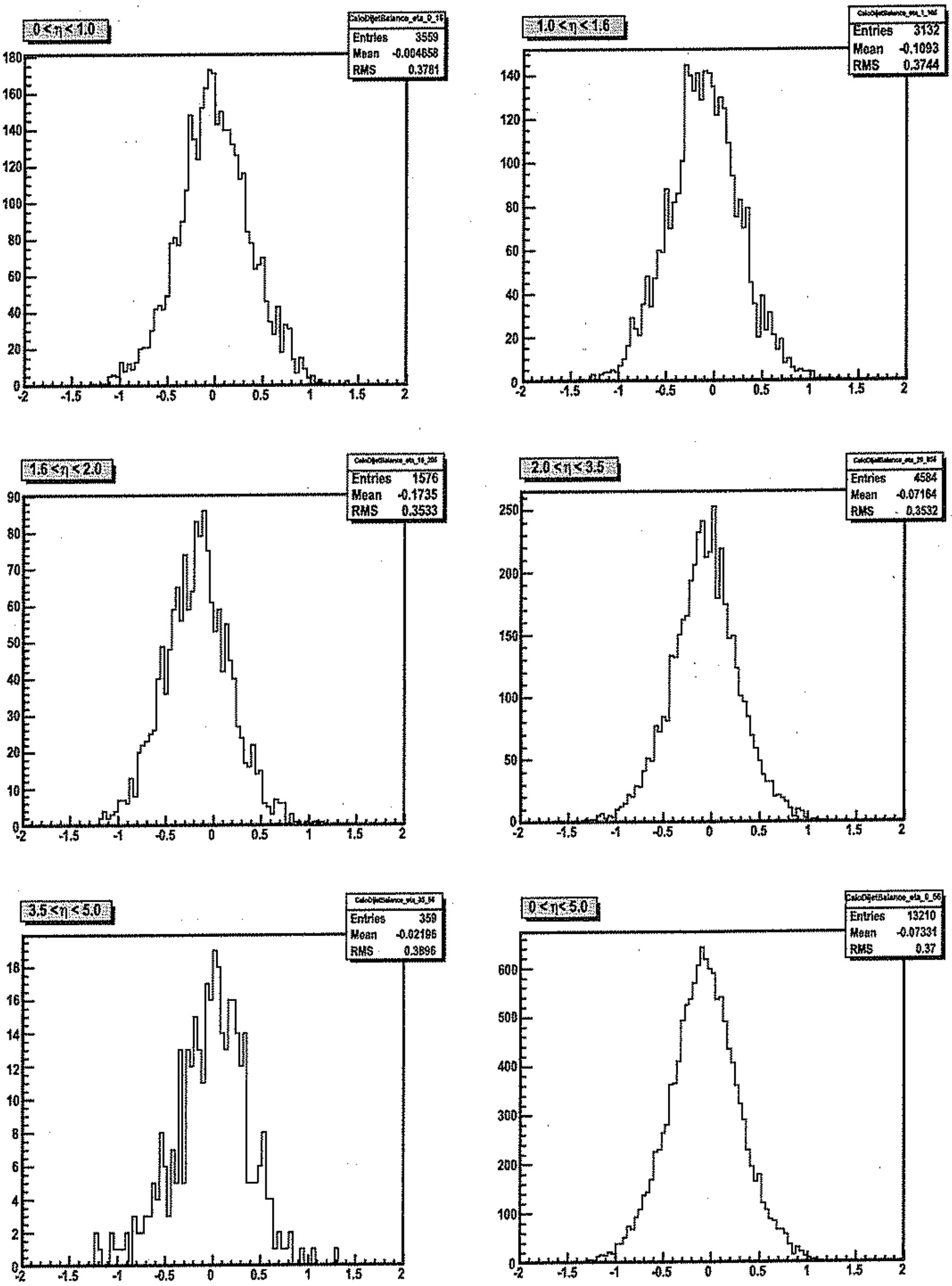

Figure 6.2 Distribution of dijet balance for different eta regions ($80 < p_T^{ave} < 120$).

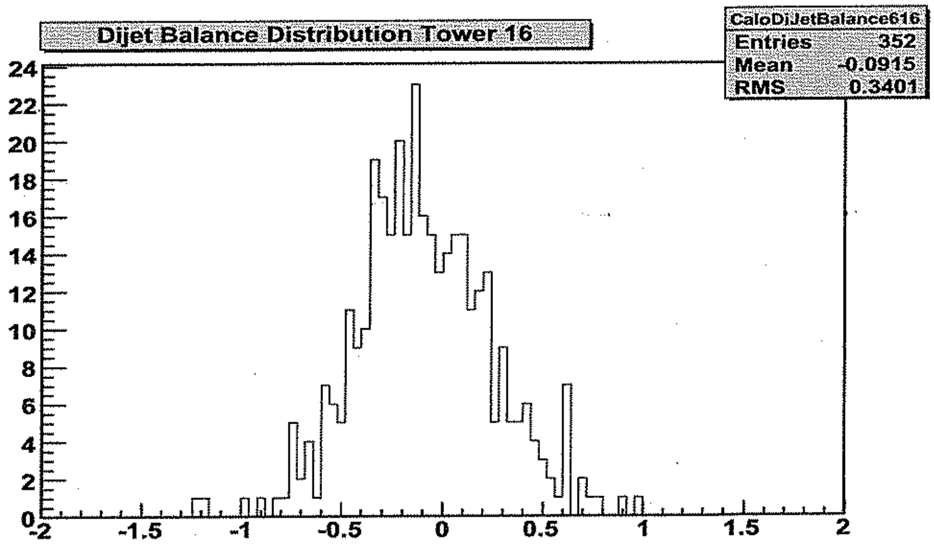

Figure 6.3 Distribution of dijet balance for tower 16.

Response measurement details;

• Divide data into bins of p_T^{ave} 30-50, 50-80, 80-120, 120-170 ... GeV

• Divide data into bins of probe jet η, and for each bin, determine from the calorimeter balance distribution (B_{PT}) and plot it.

• Get the mean of the plot using root (root is an object oriented graphical program which is developed in CERN)

• Calculate $R_{B_{PT}} = (2 + \langle B_{PT} \rangle)/(2 - \langle B_{PT} \rangle)$

• Plot $R_{B_{PT}}$ as a function of η. See fig.6.4 and 6.5 .

6.1.2 Correction

The relative energy correction is defined with dijet balancing as $1/R_{B_{PT}}$. If this method was perfect the dijet balance applied to sample after this relative energy corrections would be a flat line at 1. In figure 6.6 we compare the response versus η of corrected and uncorrected jets.

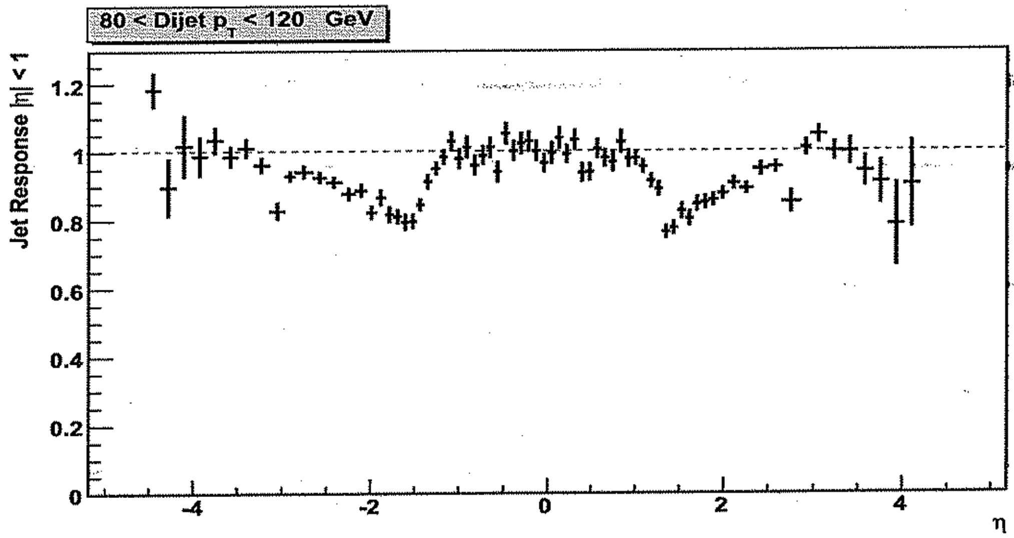

Figure 6.4 Response from dijet balancing for $80 < p_T^{ave} < 120$ GeV. The response is normalized to 1 in $0 < |\eta| < 1$ region.

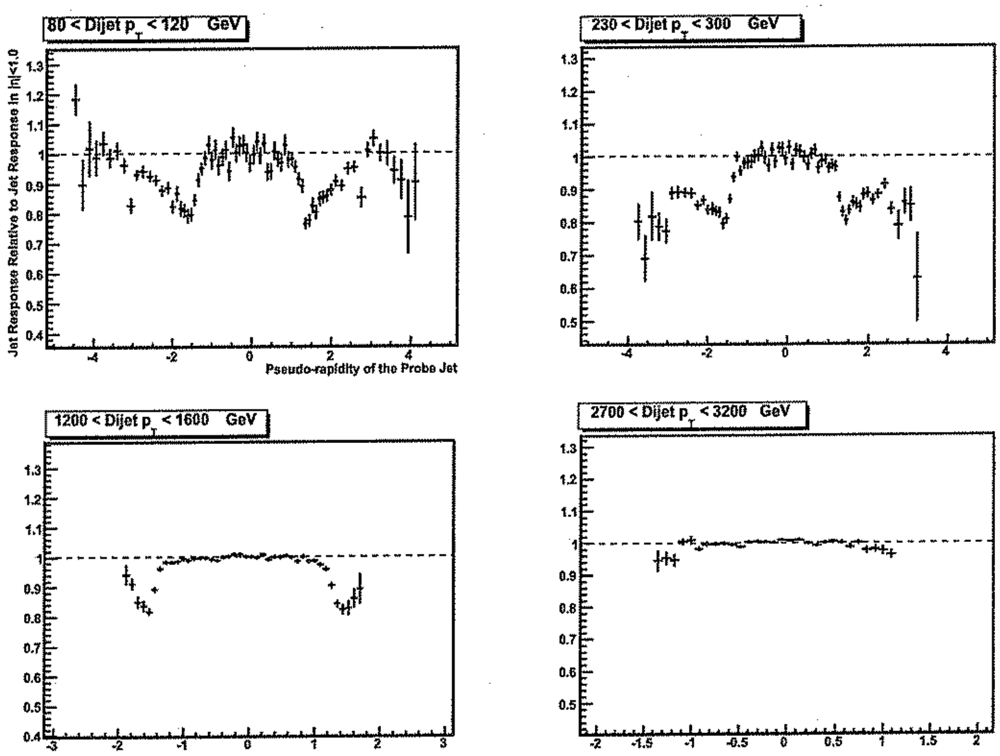

Figure 6.5 Response from dijet balancing for 4 different ranges of p_T^{ave}.

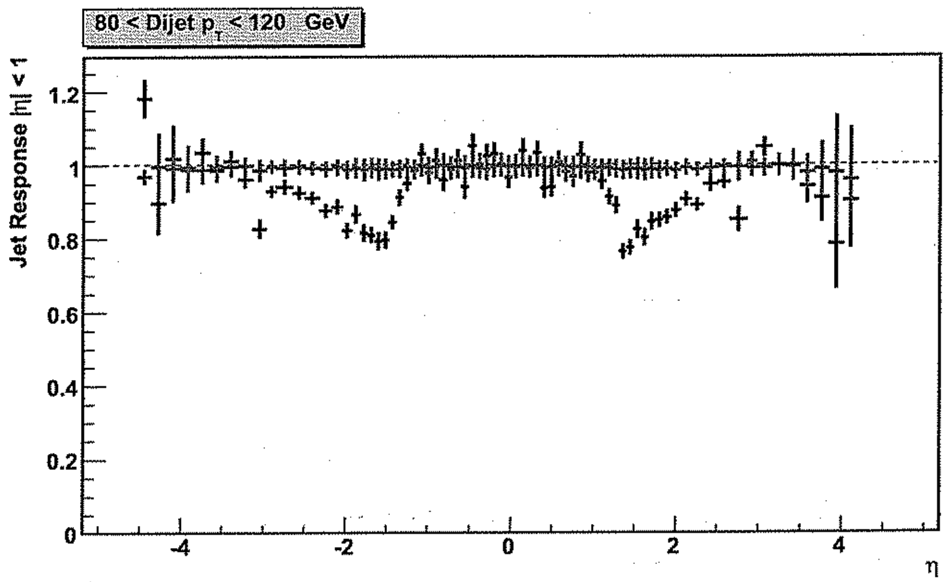

Figure 6.6 Response from Dijet Balancing of corrected jets (red) and raw jets (black) for $80 < p_T^{ave} < 120$ GeV as a function of η.

6.2 Correction Using Missing E_T Projection Fraction Method

We define the Missing E_T Projection Fraction (MPF) for two leading jets $(jet_{probe}, jet_{barrel})$ and missing E_T (MET) as follow.

$$MPF = \frac{\vec{E}_T^{miss} . \hat{p}_T^{probe}}{(p_T^{probe} + p_T^{barrel})/2} \tag{6.4}$$

We used dijet balance p_T in order to measure MPF. Here p_T selection has been made in the same way as in dijet balance (See Fig.6.1).

Main difference between MPF and dijet balance method is MET effects. In dijet balance method we didn't use the MET. Thus the MPF method is a more sensitive method than the dijet balance method.

In Fig.6.7 MPF is shown for $2700 < p_T^{ave} < 3200$ GeV for different η regions covering the whole CMS calorimeter.

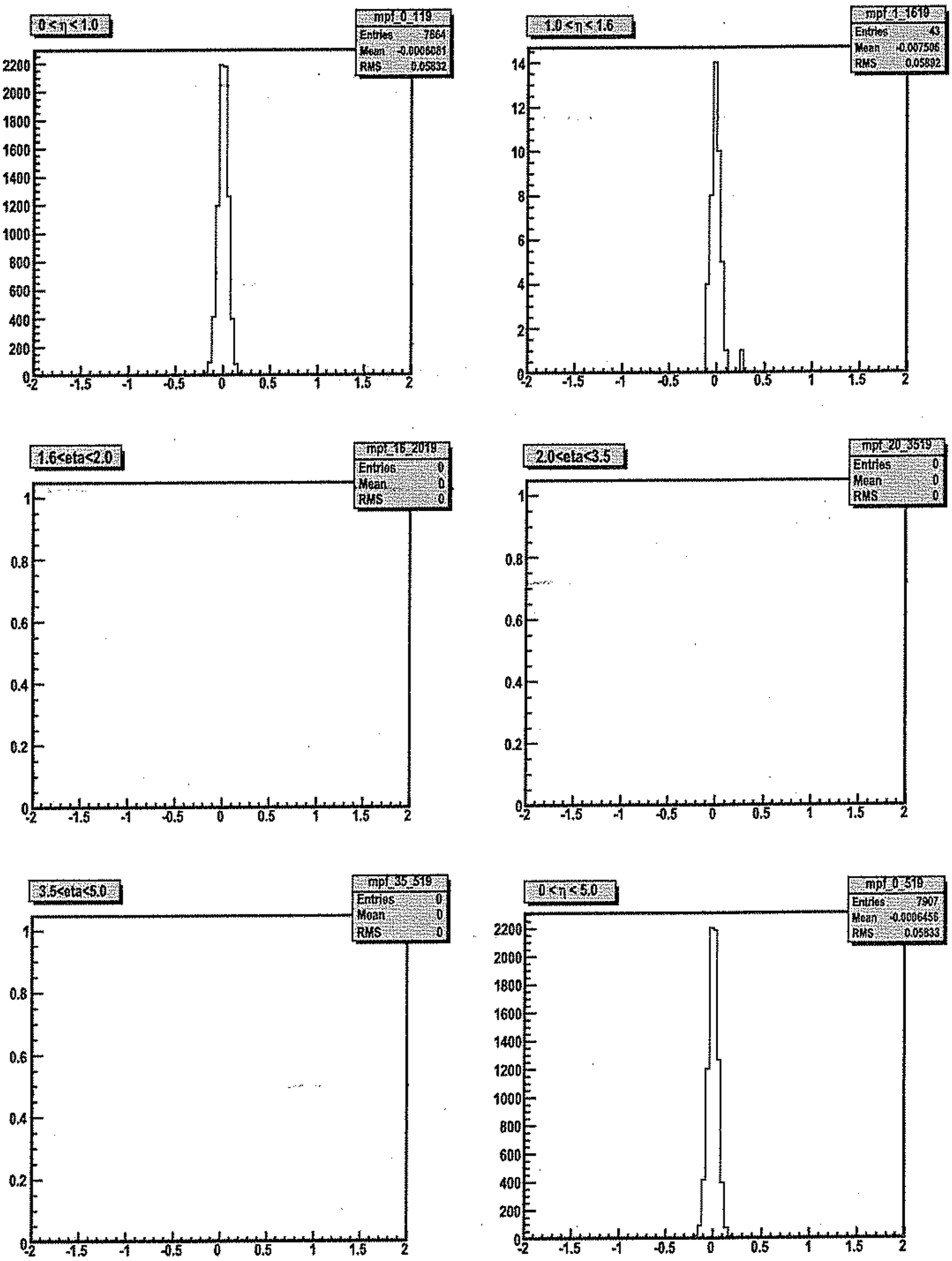

Figure 6.7 Distribution of MPF for different eta region ($2700 < p_T^{ave} < 3200$).

6.2.1 Response Measurement

If there is no soft gluon radiation and the underlying event is perfectly balanced in transverse plan,

$$\vec{E}_T^{miss}.\hat{p}_T^{probe} = p_T^{barrel} - p_T^{probe} \quad (6.5)$$

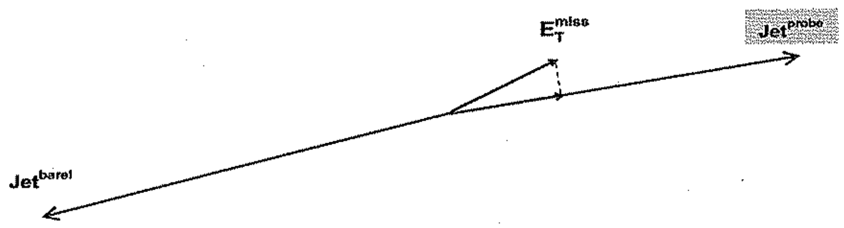

Figure 6.8 Missing E_T projection selection.

so the response is;

$$R_{MPF} = \frac{p_T^{probe}}{p_T^{barrel}} = \frac{2 - \langle MPF \rangle}{2 + \langle MPF \rangle} \quad (6.6)$$

In Fig.6.9 we show MPF distribution in tower 16. We measured the mean of MPF distribution and than response of MPF was calculated for each tower.

In Fig.6.10 we show the response versus η from MPF for $80 < Dijet p_T < 120$.

6.2.2 Correction

The jet energy is corrected by $1/R_{MPF}$. If this method was perfect the MPF applied to sample after these relative energy corrections would be a flat line at 1.

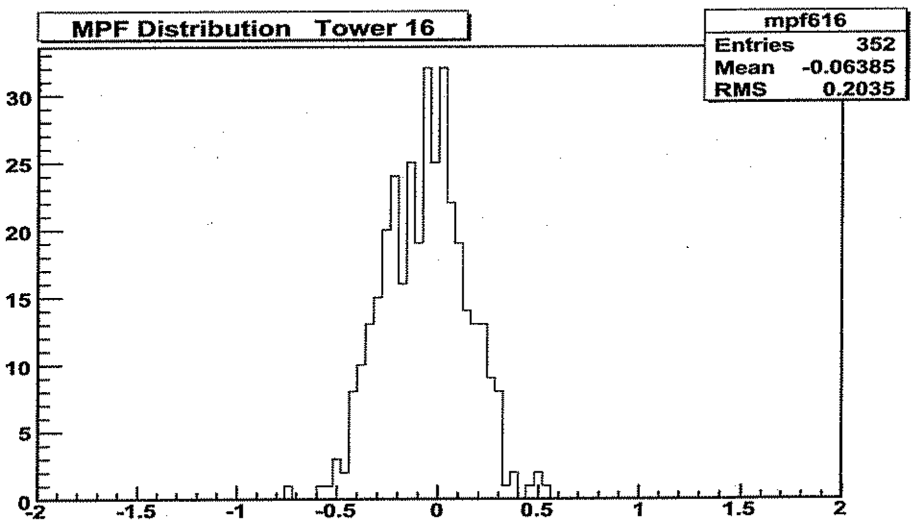

Figure 6.9 Distribution of MPF for tower 16.

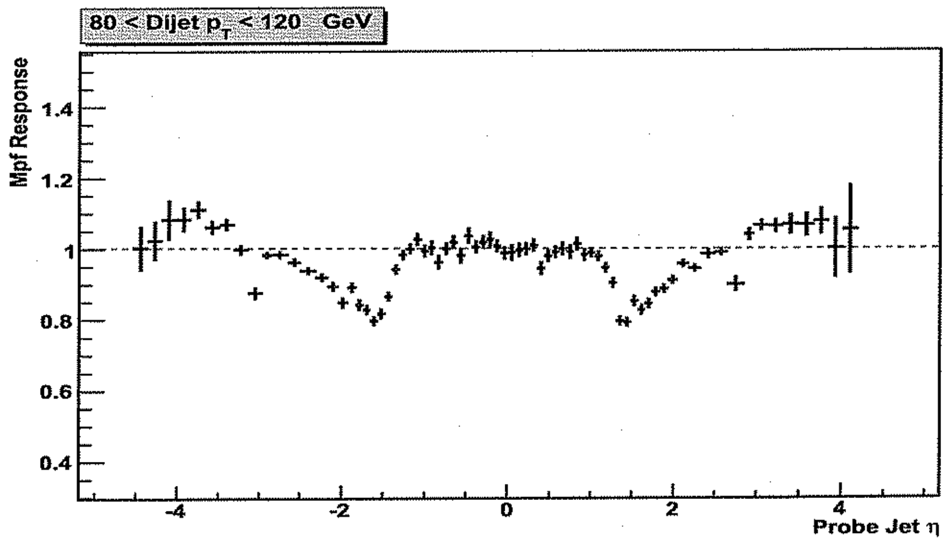

Figure 6.10 Response from *MPF* for $80 < p_T^{ave} < 120$.

6.3 Correction Using Photon-Jet Balacing Method

We used photon-jet data for analysis and selected the particle level photons p_T in the data. In Fig.6.11 we show the selection of photons p_T

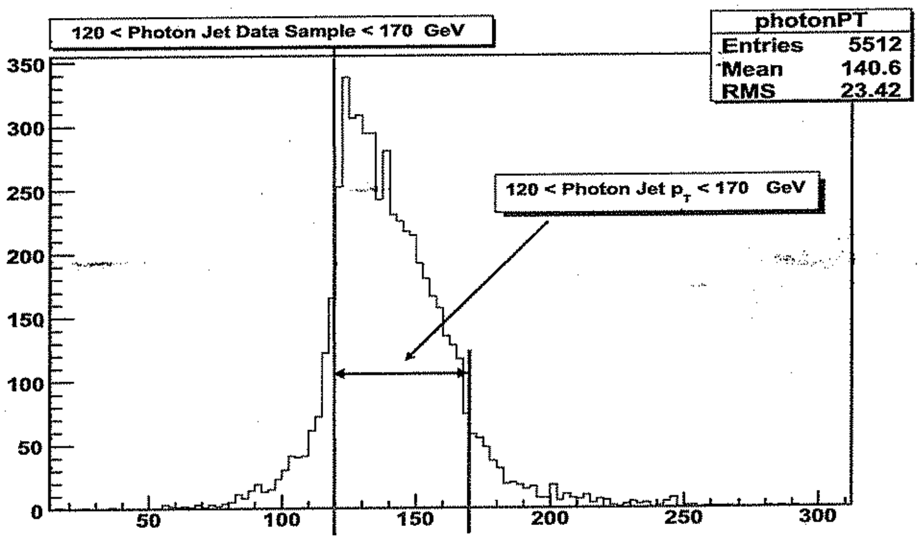

Figure 6.11 Distribution of Photons p_T. As you can see sample p_T range is equal to photons p_T range.

Photon jet balance is defined by particle level photons and calorimeter jets. We use p_T^{γ} instead of p_T^{ave} (2 leading jets average p_T) because p_T^{γ} is accurately measured and has correct absolute scale;

$$B_{\gamma} = \frac{p_T^{probe} - p_T^{photon}}{p_T^{\gamma}} \tag{6.7}$$

In Fig.6.12 distribution of photon jet balance with different η range is shown. Here p_T is from 120 to 170 GeV. As can be seen from figure distribution of photon-jet balance is arround 0.4 because of using particle level photons.

As reconstructed photons in CMSSW are not fully understood, we use the photon from particle list.

6.3.1 Response Measurement

We calculated the photon jet response with following formula;

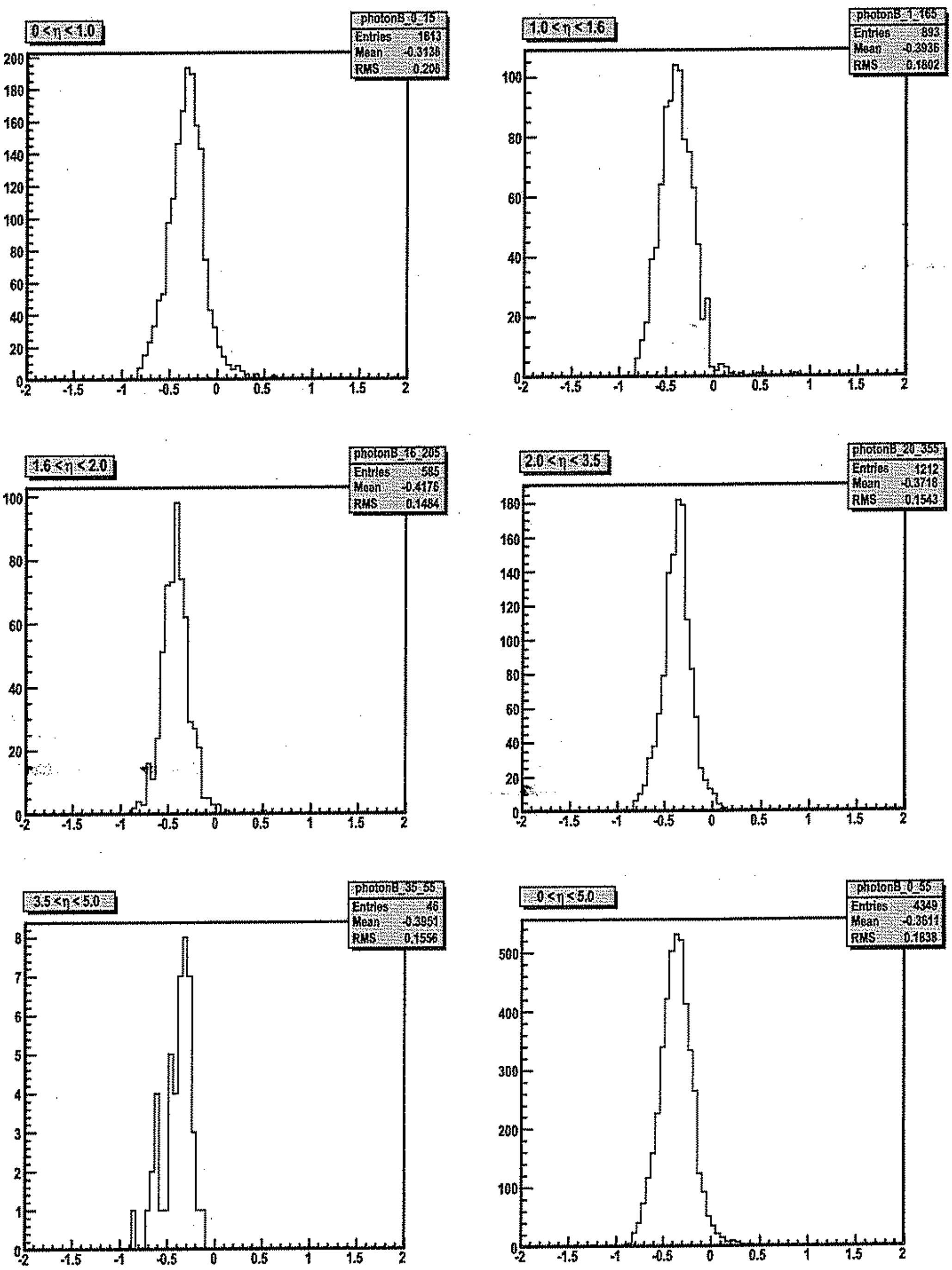

Figure 6.12 Distribution of the photon-jet balance for $120 < p_T^{\gamma} < 170$ GeV.

$$R_{B_\gamma} = \frac{p_T^{probe}}{p_T^{barel}} = \frac{2 + \langle B_\gamma \rangle}{2 - \langle B_\gamma \rangle} \tag{6.8}$$

First we got the mean value of the photon jet balance for each tower (see Fig.6.13). Than we used above formula and calculated the response for each of 82 towers.

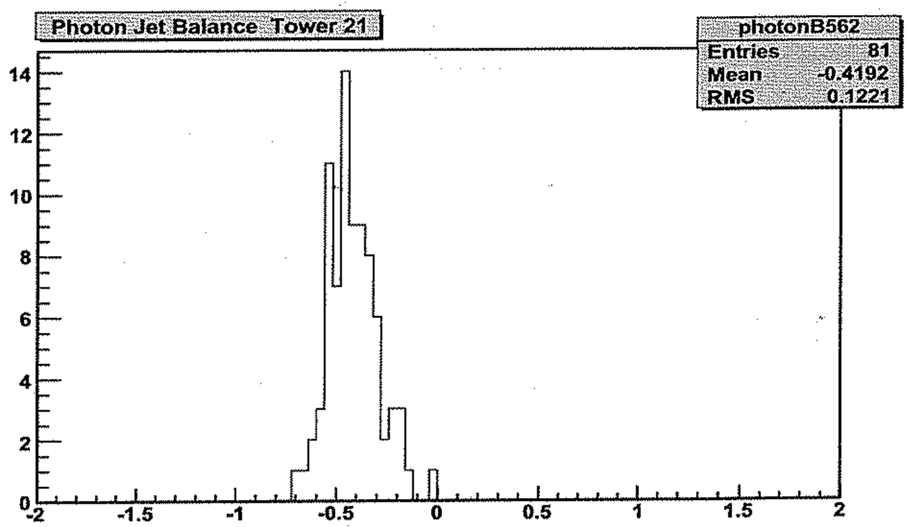

Figure 6.13 Photon-jet balance tower 21.

6.3.2 Correction

In Fig.6.14 is shown response of photon jet versus η region.

The relative energy corrections are defined with photon-jet balance as $1/R_{B_\gamma}$. If this method was perfect the photon-jet balance applied to sample after these relative energy corrections would be a flat line at 0.65 because we use particle level photons.

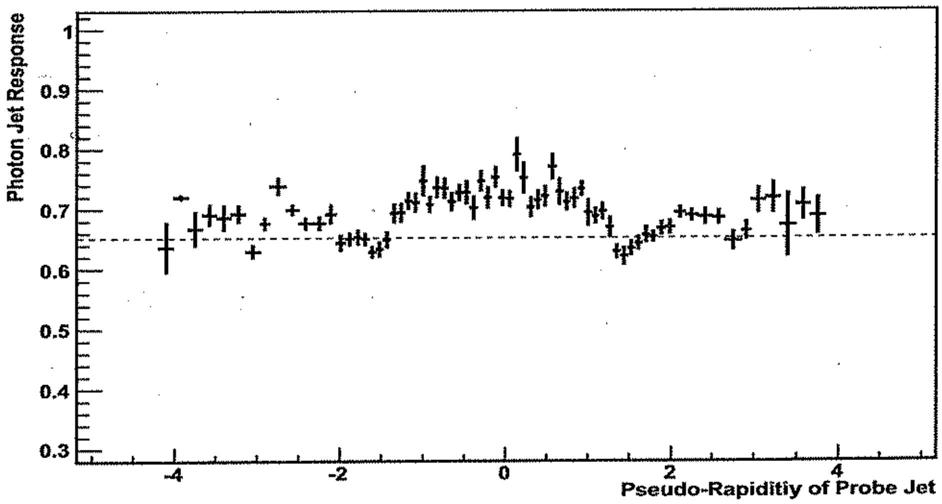

Figure 6.14 Photon-jet response versus η for $120 < p_T^\gamma < 170$ GeV.

7. COMPARISON

7.1 Comparison of the Dijet Balance and Missing E_T Projection Fraction

In this section, comparisons between the relative jet energy corrections using the dijet balance and MPF methods are presented. The dijet balance and MPF are defined in section 6.1 and 6.2 repectively.

7.1.1 Shape of the Dijet Balance and MPF Distribution

Figure 7.1 shows $-MPF$ and dijet balance distributions for the different detector-η bins in the CSA06 data (cone size R=0.5). For all of the detector-η bins, MPF distributions are narrower than dijet balance distributions. Fig. 7.2 shows the larger version of one of the plots in the figure 7.1 and the RMS of the MPF and dijet balance distributions as a function of detector-η. The RMS of the MPF is smaller than that of the dijet balance distribution by roughly 20% for the cone size of $R = 0.5$.

7.1.2 Shape of Response from Dijet Balance and MPF

Fig. 7.3 shows response from the MPF and dijet balance distributions as a function of detector-η. When there is no gluon radiation $dB = -MPF$, therefore, in this section we compared the MPF and dijet balance response versus detector-η bins. Shapes of these two plots are very similar. In large η regions shape is different because in dijet balance we didn't use MET. MPF is expected be less dependent on how well the third jet is clustered and results are better than dijet balancing resolution.

7.1.3 For Different Cone Sizes

Figure 7.4 are the same as figures 7.2 and 7.3 but for the cone size of $R = 0.7$. In both cases, the RMS of the MPF distributions is again smaller than that of the dijet distributions. The difference in the RMS is about 18% for the cone size $R = 0.7$. This can be explained by the fact that the smaller cone size is more sensitive to the soft gluon radiation.

7.1.4 For Different jet p_T

In this section the *MPF* and dijet balance distributions, and also their RMS were compared as a function of detector-η and response for $80 < p_T^{ave} < 380$ GeV, results are shown in figures 7.5 - 7.18.

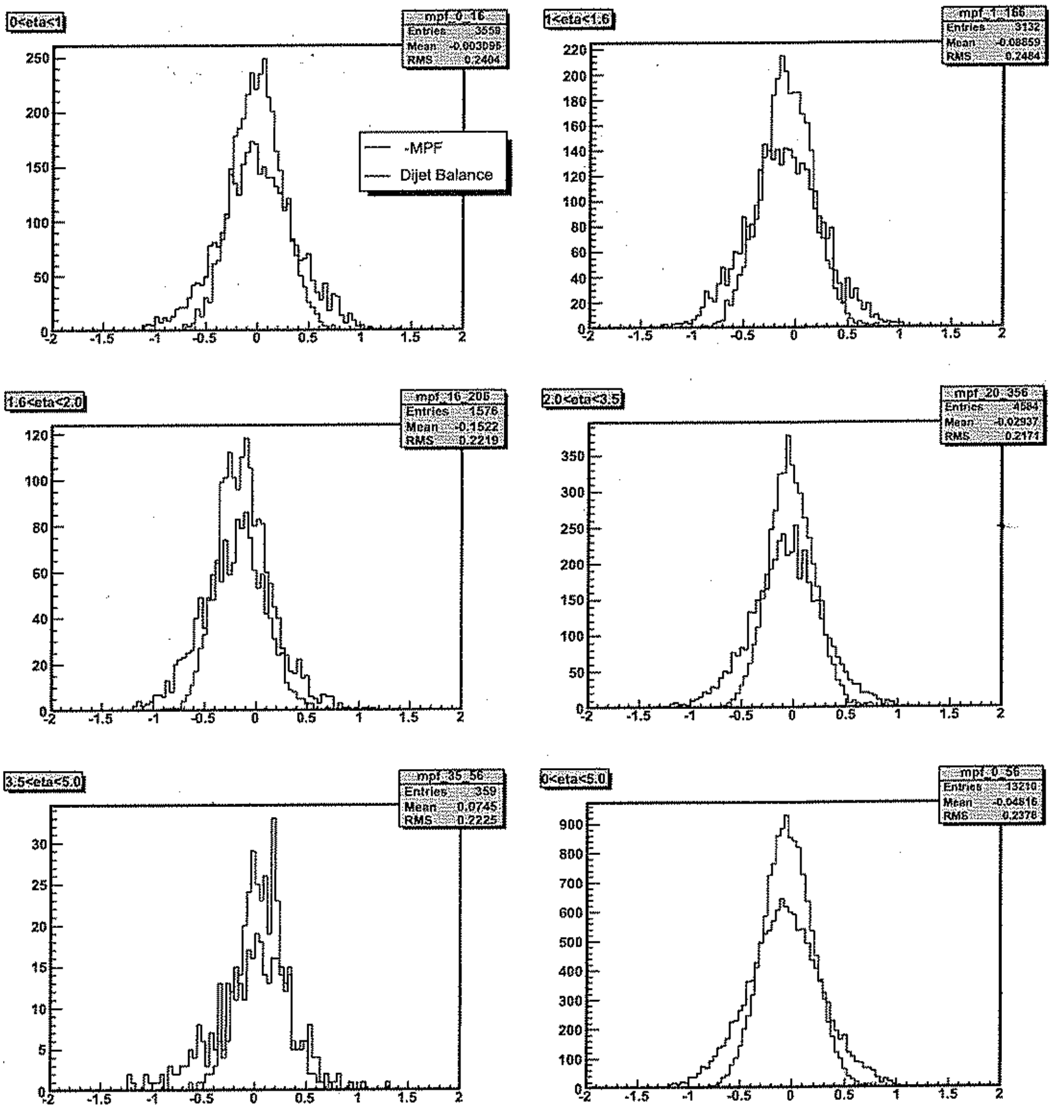

Figure 7.1 Distribution of $-MPF$ and dijet balance for different detector-η bins (Cone size $R = 0.5$), $120 < p_T^{ave} < 170$ GeV .

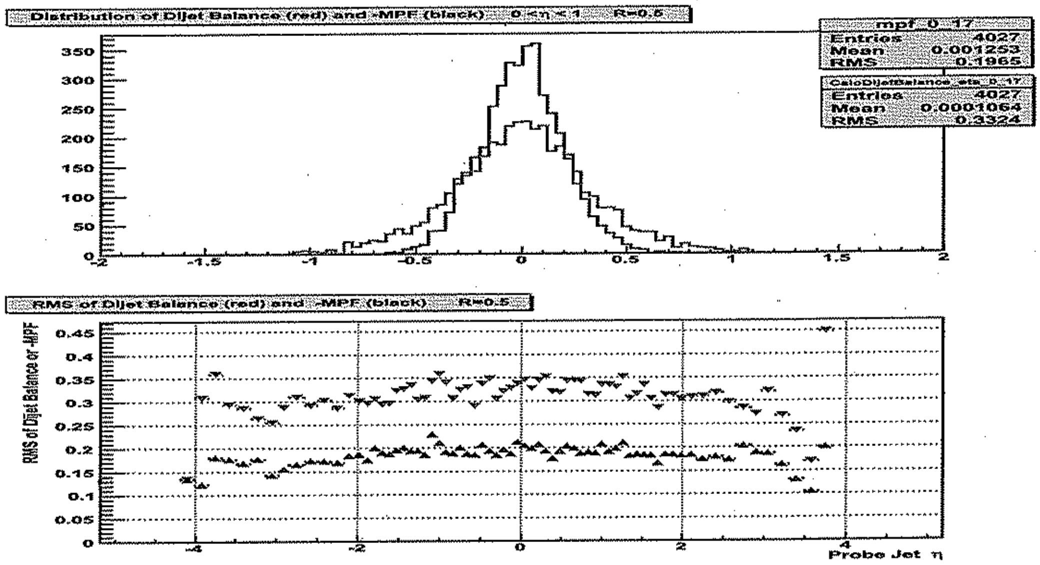

Figure 7.2 Distribution of $-MPF$ and dijet balance in detector-η bin of $|\eta| < 1.0$ (top). RMS of the MPF and dijet balance distributions as a function of detector-η (bottom). In both cases $R = 0.5$ cone were used.

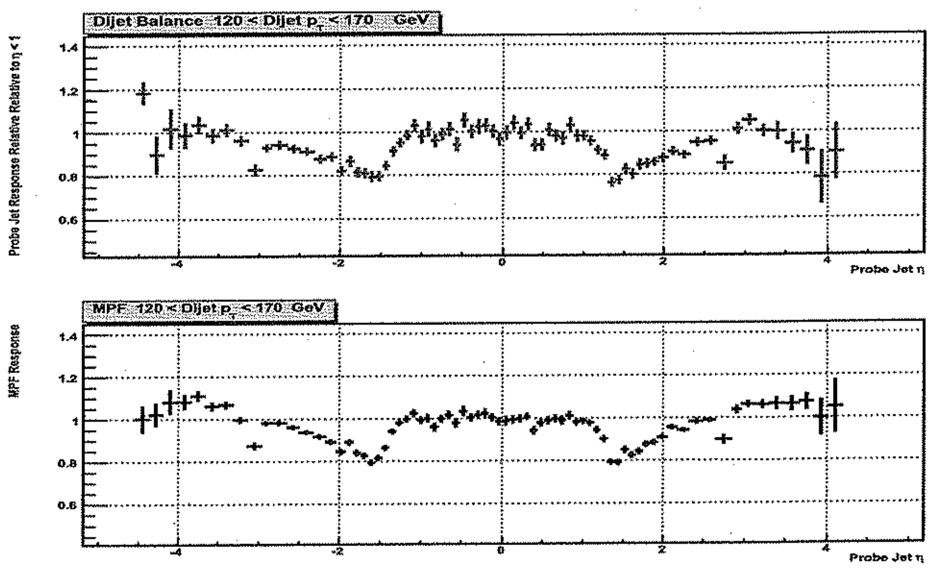

Figure 7.3 Dijet balance Response in detector-η bins (top). MPF Response in detector-η bins (bottom). In both cases $R = 0.5$ cone were used.

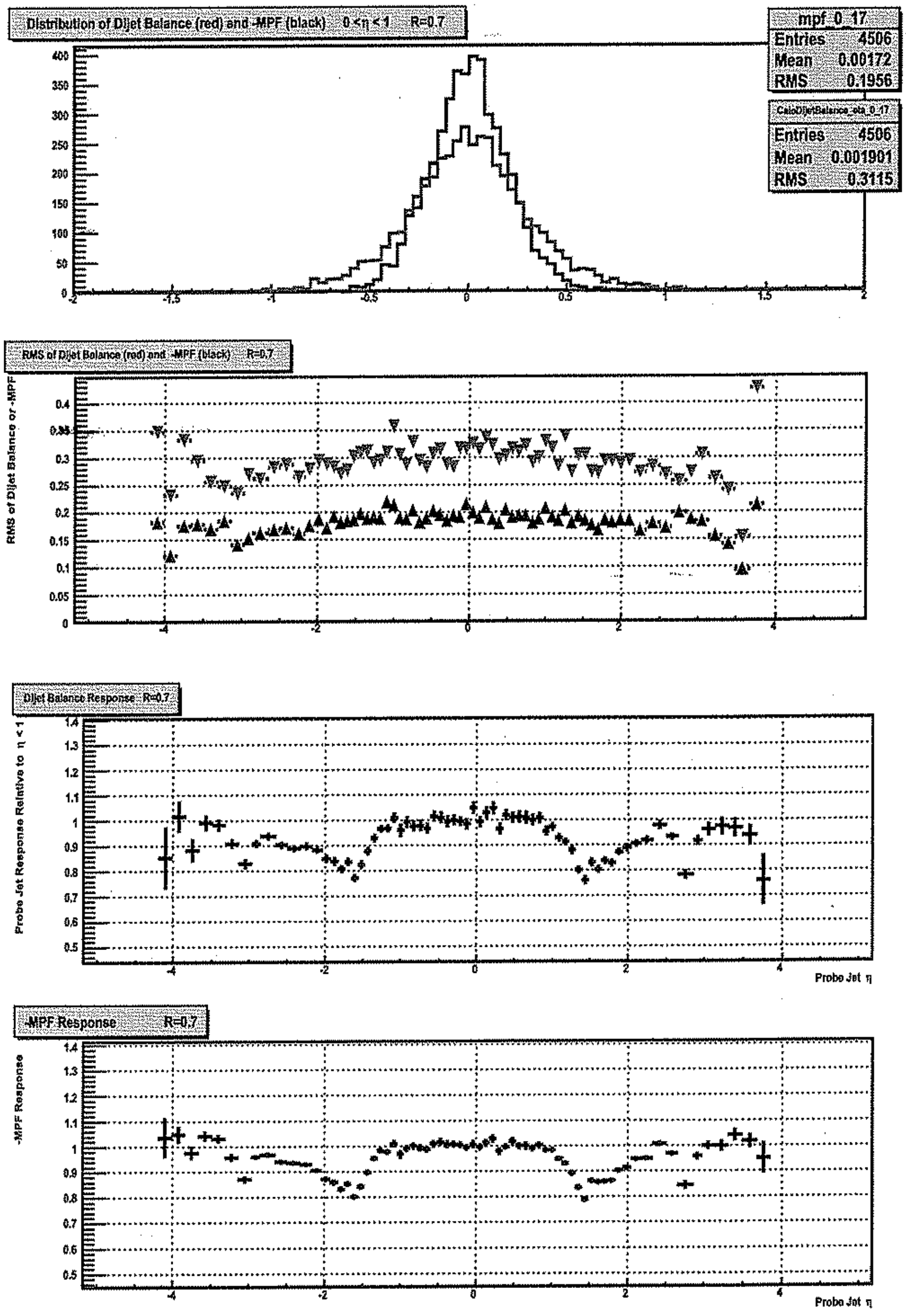

Figure 7.4 Distribution of $-MPF$ and dijet balance in detector-η bin of $|\eta| < 1.0$ (top). RMS of the MPF and dijet balance distributions as a function of detector-η (middle). Dijet balance and MPF Response in detector-η bins (bottom). All figures are for cone size $R = 0.7$.

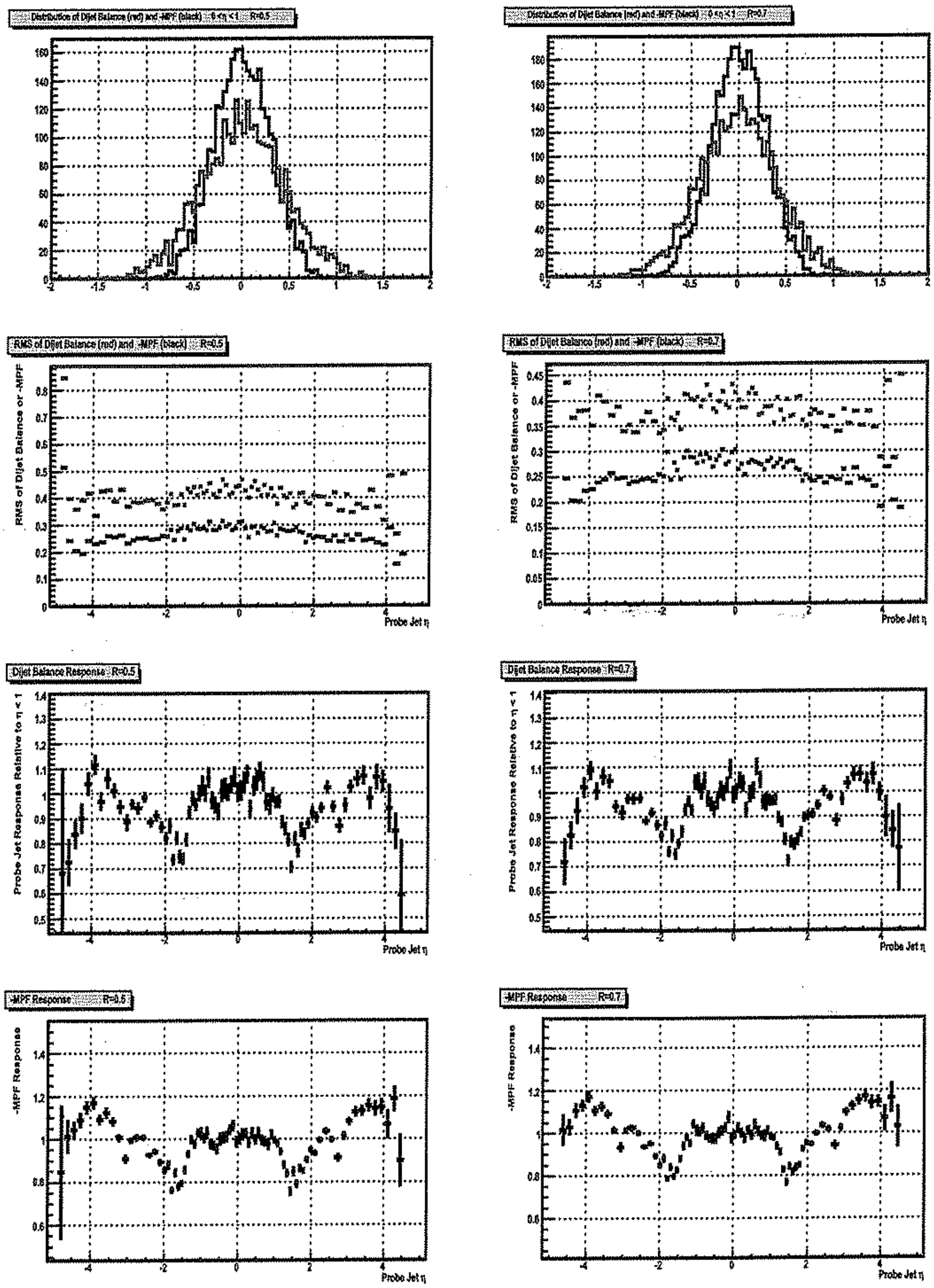

Figure 7.5 Distribution of the $-MPF$ and dijet balance in the detector-η bin of $|\eta| < 1$ (top). RMS of the dijet balance and MPF distribution as a function of detector-η for the $50 < p_T^{ave} < 80$ (middle). MPF and dijet balance response in detector-η bins (bottom). Cone size $R = 0.5$ (left plots). Cone size $R = 0.7$ (right plots).

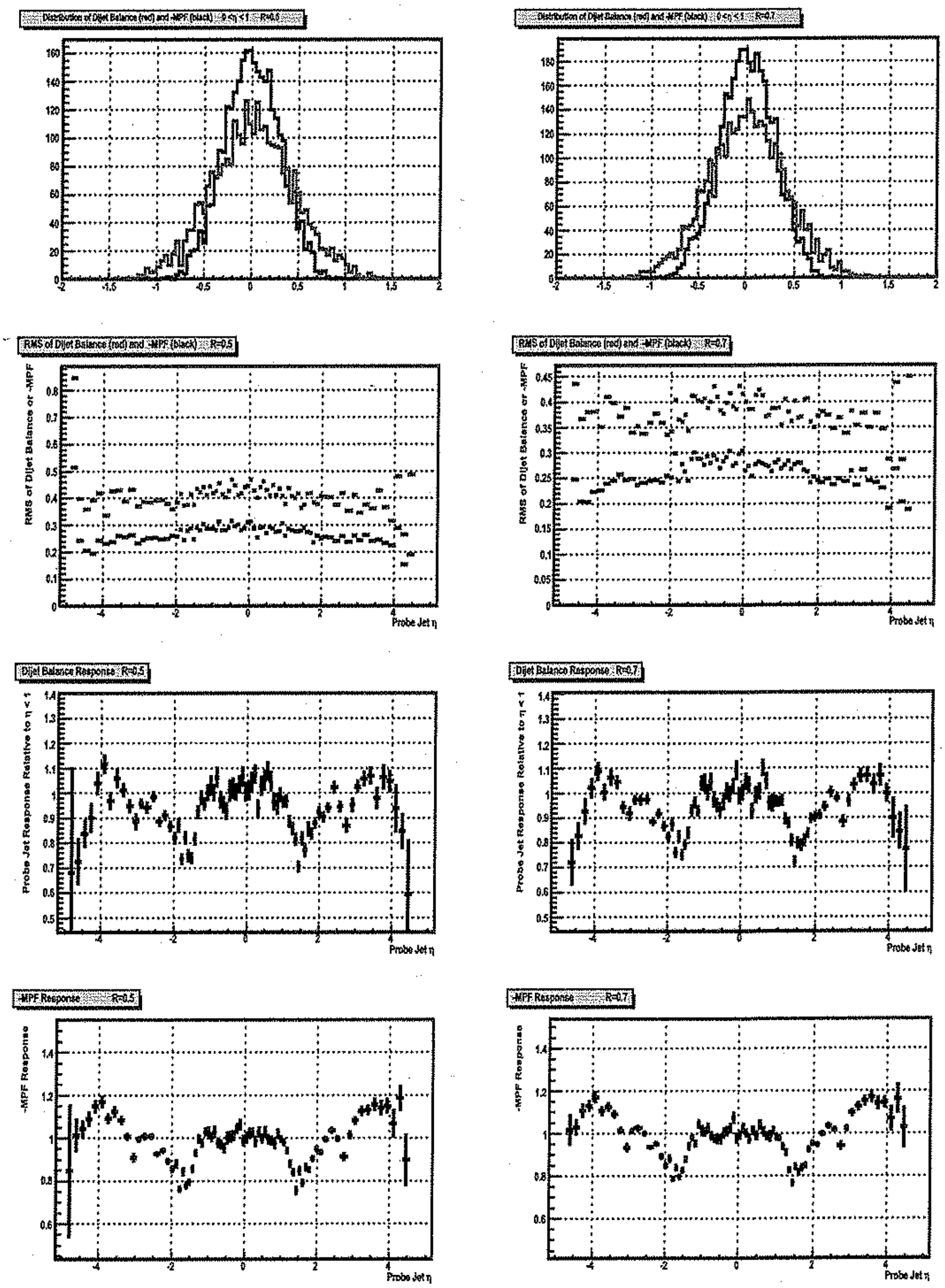

Figure 7.6 Distribution of the $-MPF$ and dijet balance in the detector-η bin of $|\eta| < 1$ (top). RMS of the dijet balance and MPF distribution as a function of detector-η for the $80 < p_T^{ave} < 120$ (middle). MPF and dijet balance response in detector-η bins (bottom). Cone size $R = 0.5$ (left plots). Cone size $R = 0.7$ (right plots).

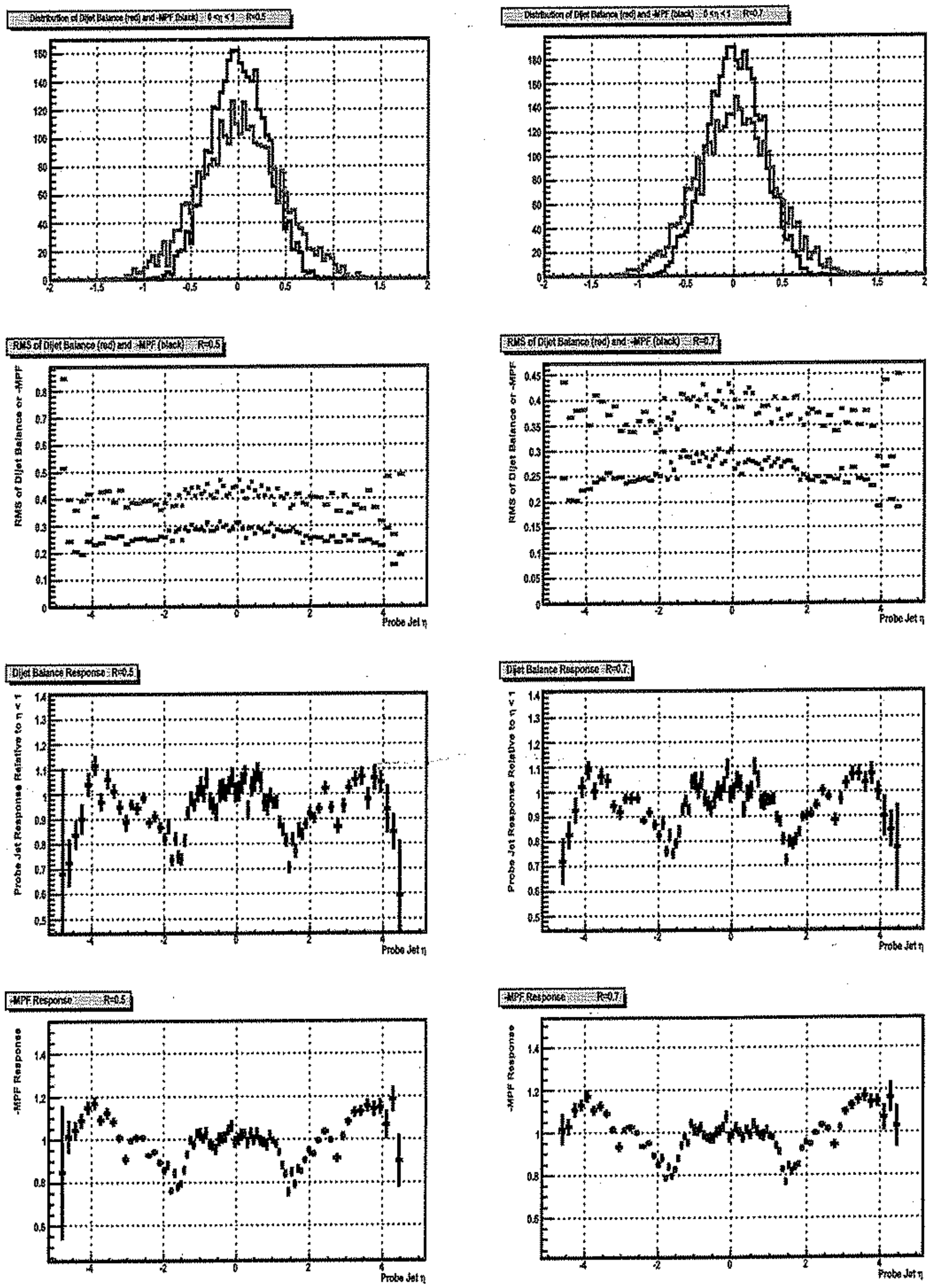

Figure 7.7 Distribution of the $-MPF$ and dijet balance in the detector-η bin of $|\eta| < 1$ (top). RMS of the dijet balance and MPF distribution as a function of detector-η for the $120 < p_T^{ave} < 170$ (middle). MPF and dijet balance response in detector-η bins (bottom). Cone size $R = 0.5$ (left plots). Cone size $R = 0.7$ (right plots).

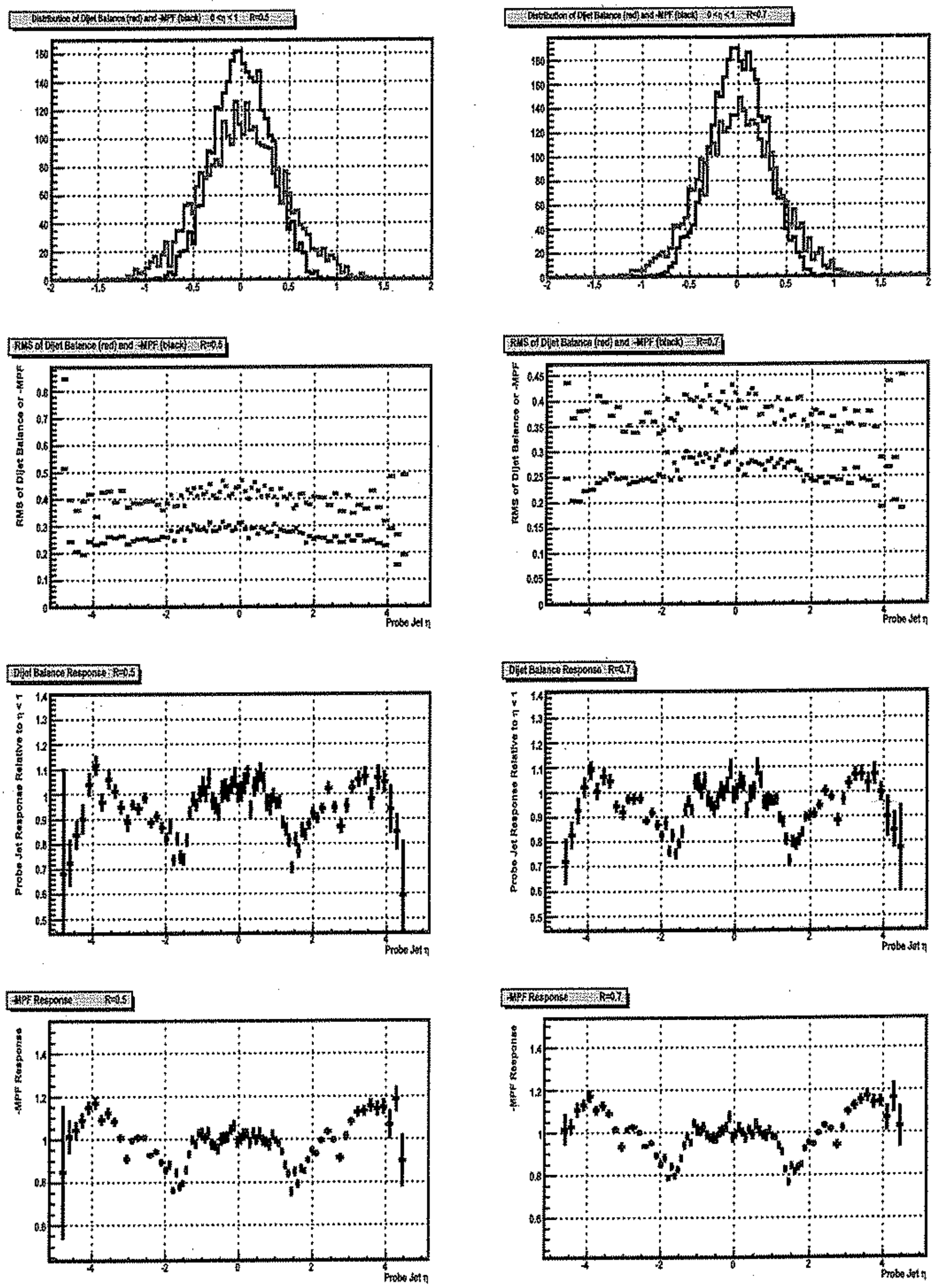

Figure 7.8 Distribution of the $-MPF$ and dijet balance in the detector-η bin of $|\eta| < 1$ (top). RMS of the dijet balance and MPF distribution as a function of detector-η for the $170 < p_T^{ave} < 230$ (middle). MPF and dijet balance response in detector-η bins (bottom). Cone size $R = 0.5$ (left plots). Cone size $R = 0.7$ (right plots).

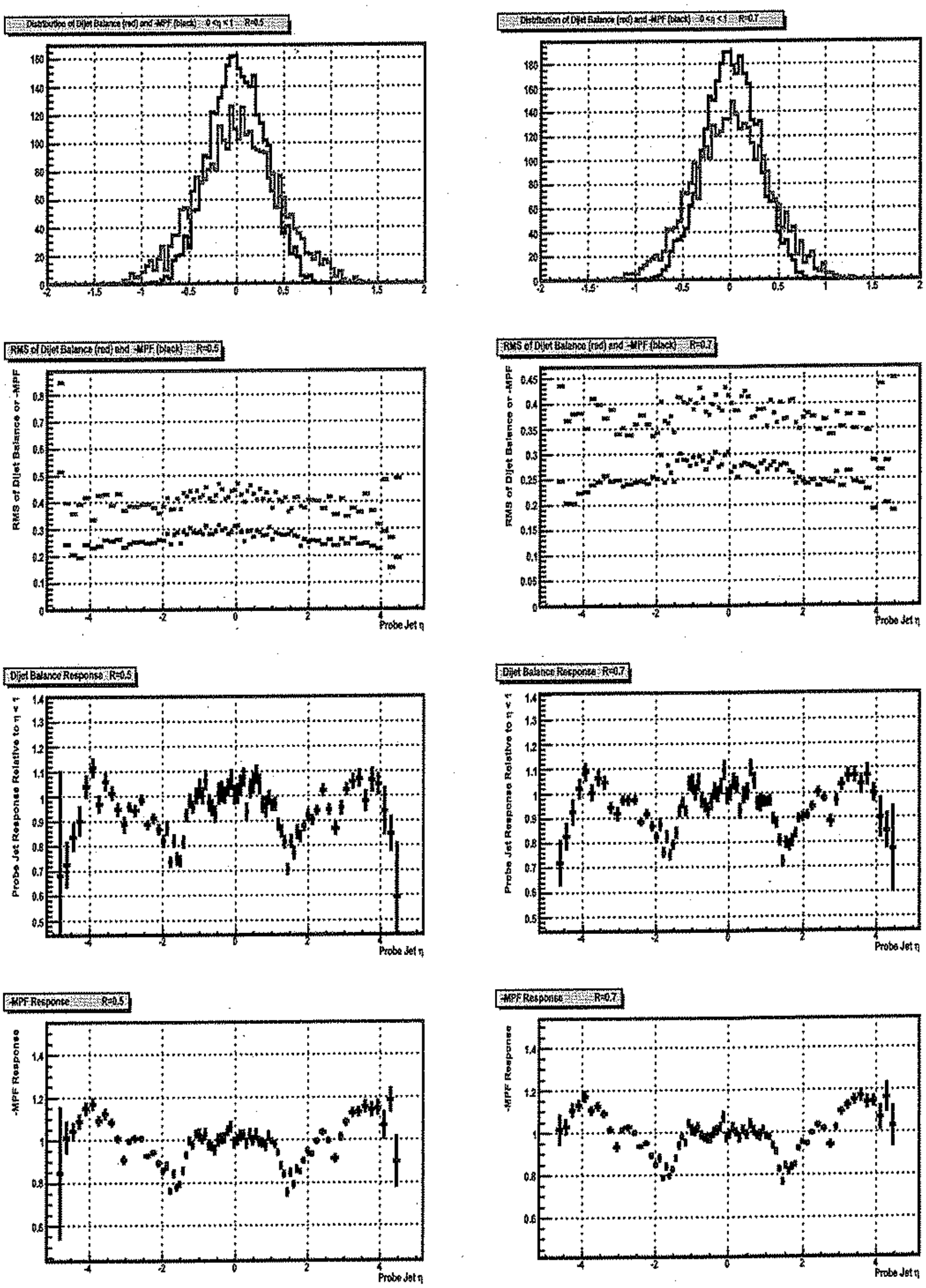

Figure 7.9 Distribution of the $-MPF$ and dijet balance in the detector-η bin of $|\eta| < 1$ (top). RMS of the dijet balance and MPF distribution as a function of detector-η for the $230 < p_T^{ave} < 300$ (middle). MPF and dijet balance response in detector-η bins (bottom). Cone size $R = 0.5$ (left plots). Cone size $R = 0.7$ (right plots).

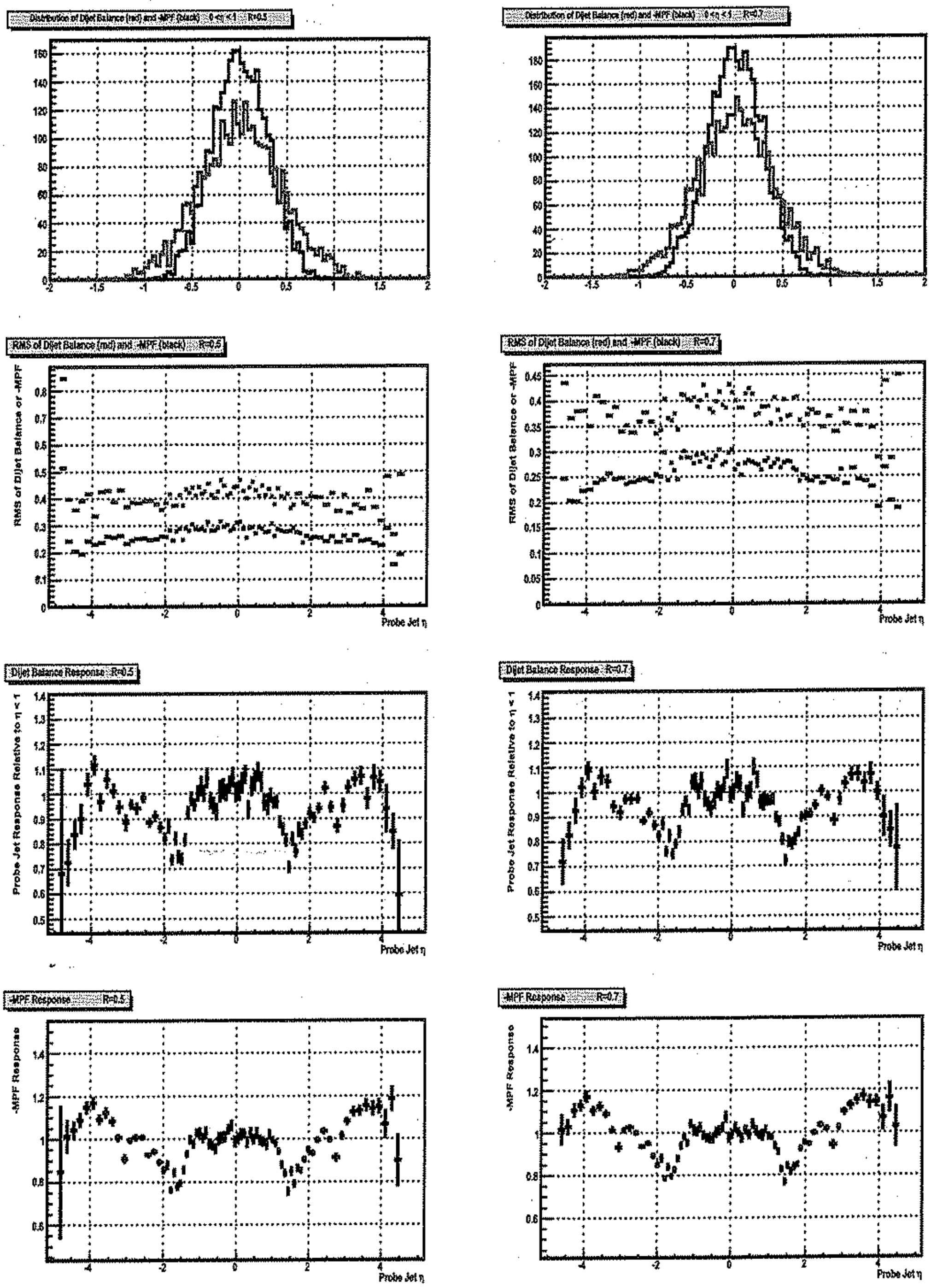

Figure 7.10 Distribution of the $-MPF$ and dijet balance in the detector-η bin of $|\eta| < 1$ (top). RMS of the dijet balance and MPF distribution as a function of detector-η for the $300 < p_T^{ave} < 380$ (middle). MPF and dijet balance response in detector-η bins (bottom). Cone size $R = 0.5$ (left plots). Cone size $R = 0.7$ (right plots).

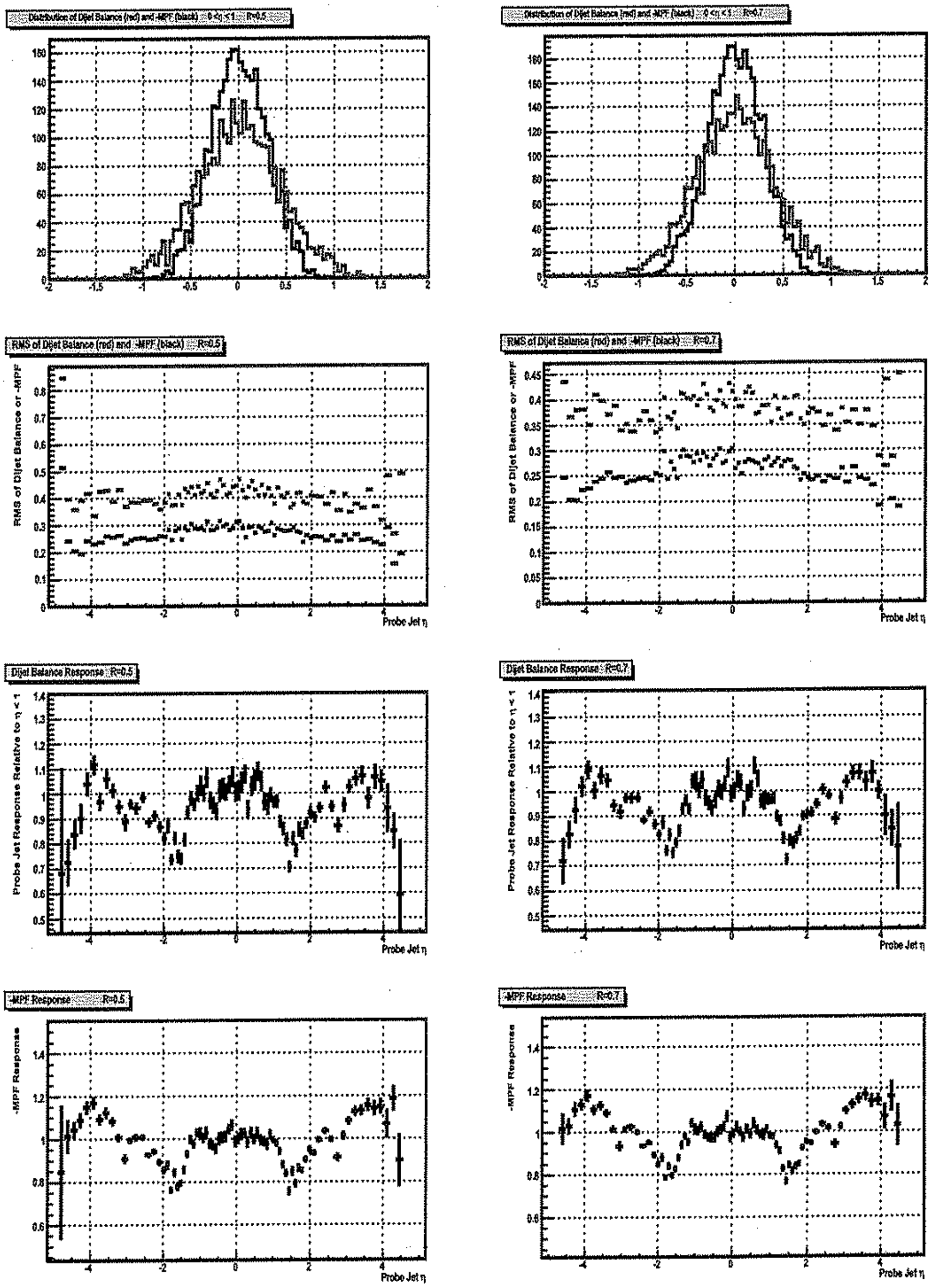

Figure 7.11 Distribution of the $-MPF$ and dijet balance in the detector-η bin of $|\eta| < 1$ (top). RMS of the dijet balance and MPF distribution as a function of detector-η for the $380 < p_T^{ave} < 500$ (middle). MPF and dijet balance response in detector-η bins (bottom). Cone size $R = 0.5$ (left plots). Cone size $R = 0.7$ (right plots).

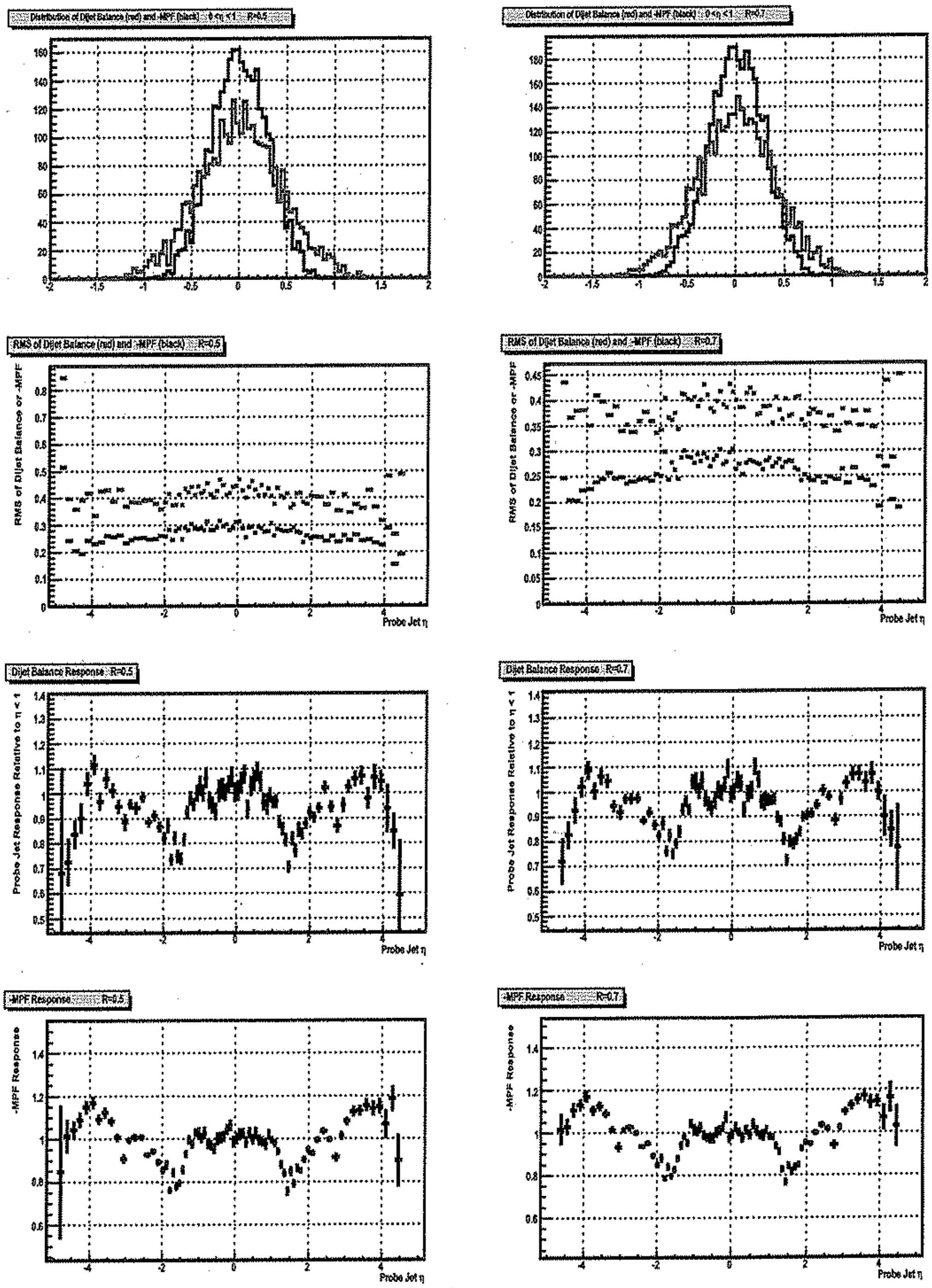

Figure 7.12 Distribution of the $-MPF$ and dijet balance in the detector-η bin of $|\eta| < 1$ (top). RMS of the dijet balance and MPF distribution as a function of detector-η for the $500 < p_T^{ave} < 700$ (middle). MPF and dijet balance response in detector-η bins (bottom). Cone size $R = 0.5$ (left plots). Cone size $R = 0.7$ (right plots).

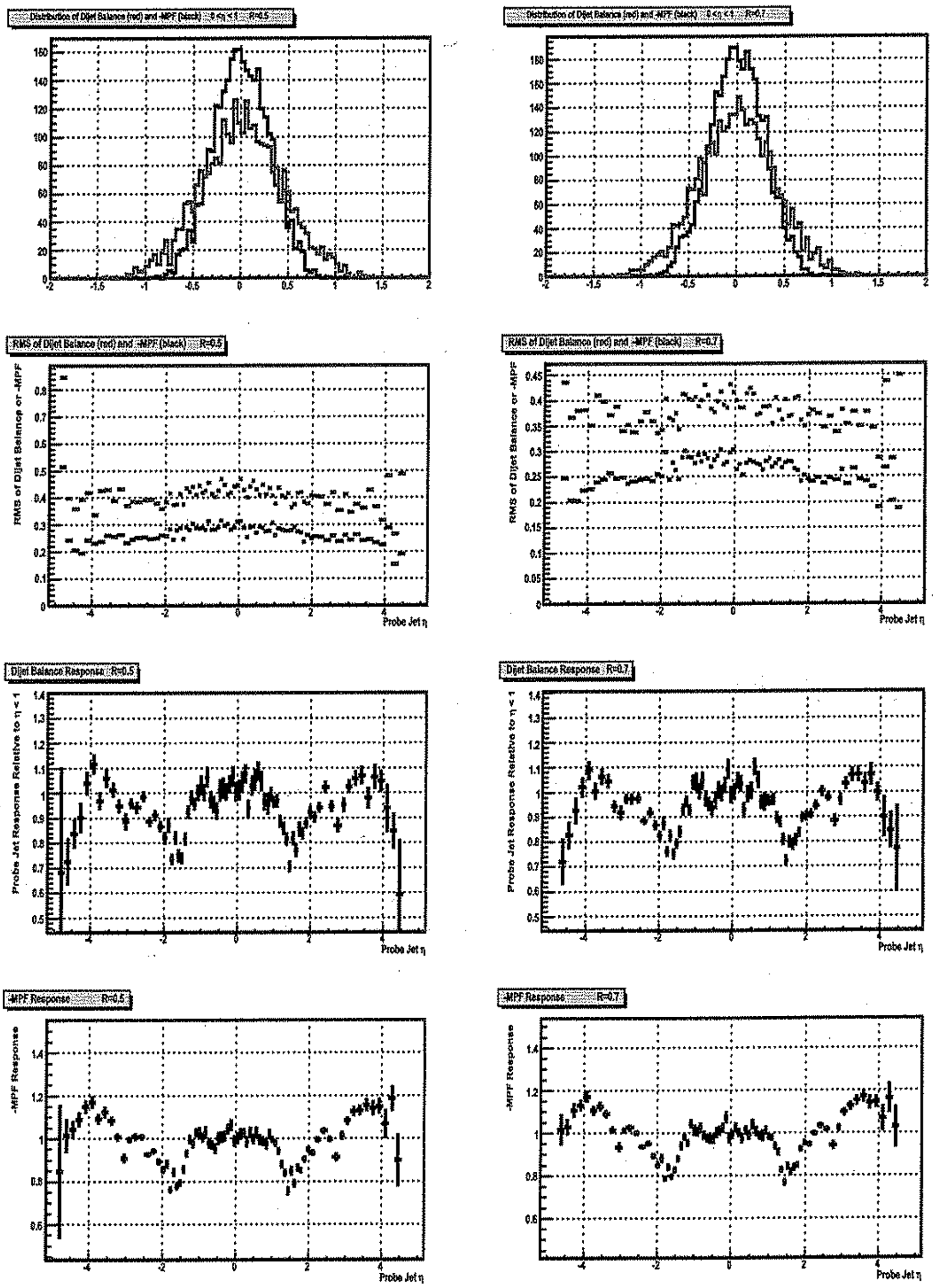

Figure 7.13 Distribution of the $-MPF$ and dijet balance in the detector-η bin of $|\eta| < 1$ (top). RMS of the dijet balance and MPF distribution as a function of detector-η for the $700 < p_T^{ave} < 900$ (middle). MPF and dijet balance response in detector-η bins (bottom). Cone size $R = 0.5$ (left plots). Cone size $R = 0.7$ (right plots).

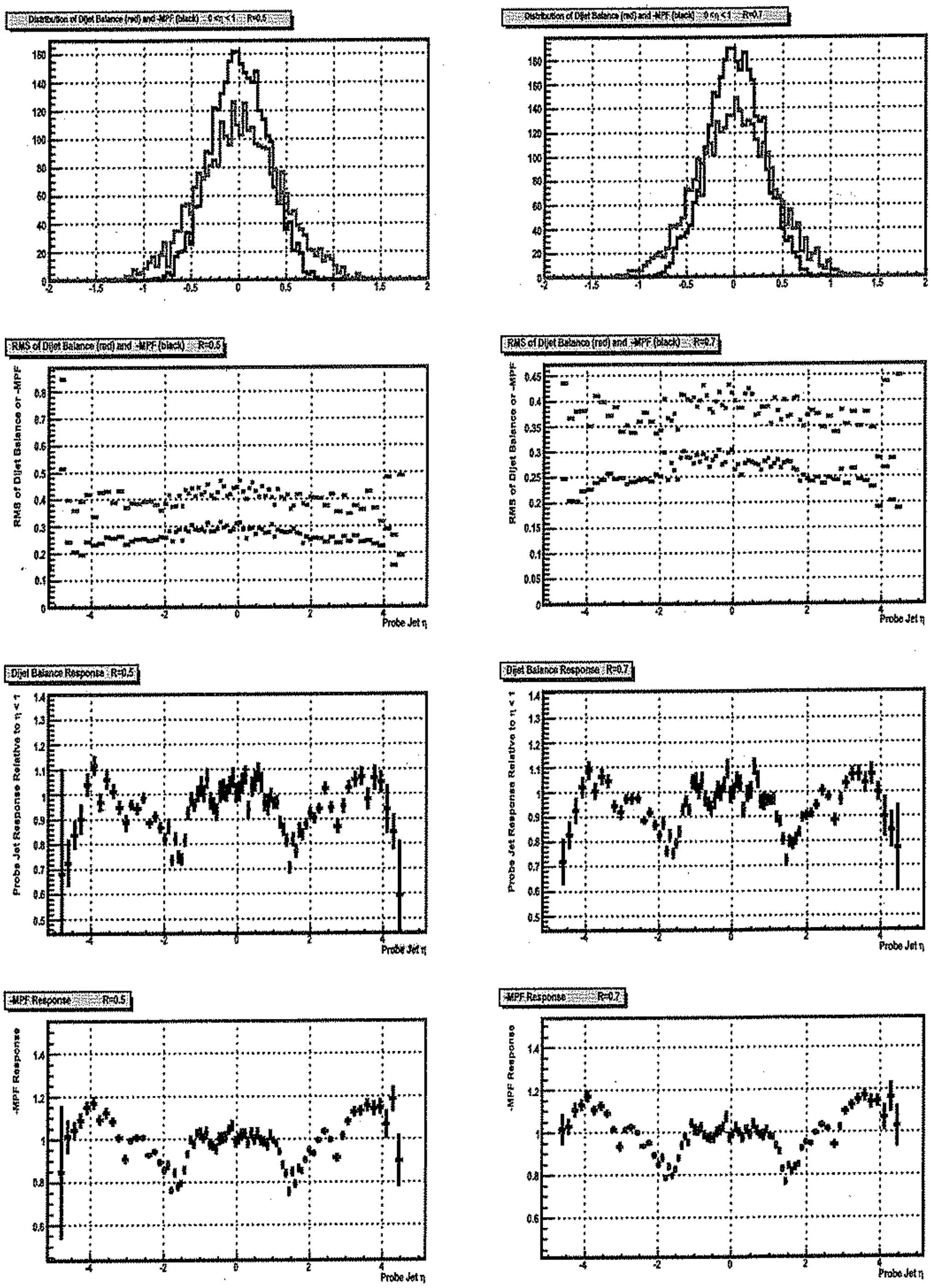

Figure 7.14 Distribution of the $-MPF$ and dijet balance in the detector-η bin of $|\eta| < 1$ (top). RMS of the dijet balance and MPF distribution as a function of detector-η for the $900 < p_T^{ave} < 1200$ (middle). MPF and dijet balance response in detector-η bins (bottom). Cone size $R = 0.5$ (left plots). Cone size $R = 0.7$ (right plots).

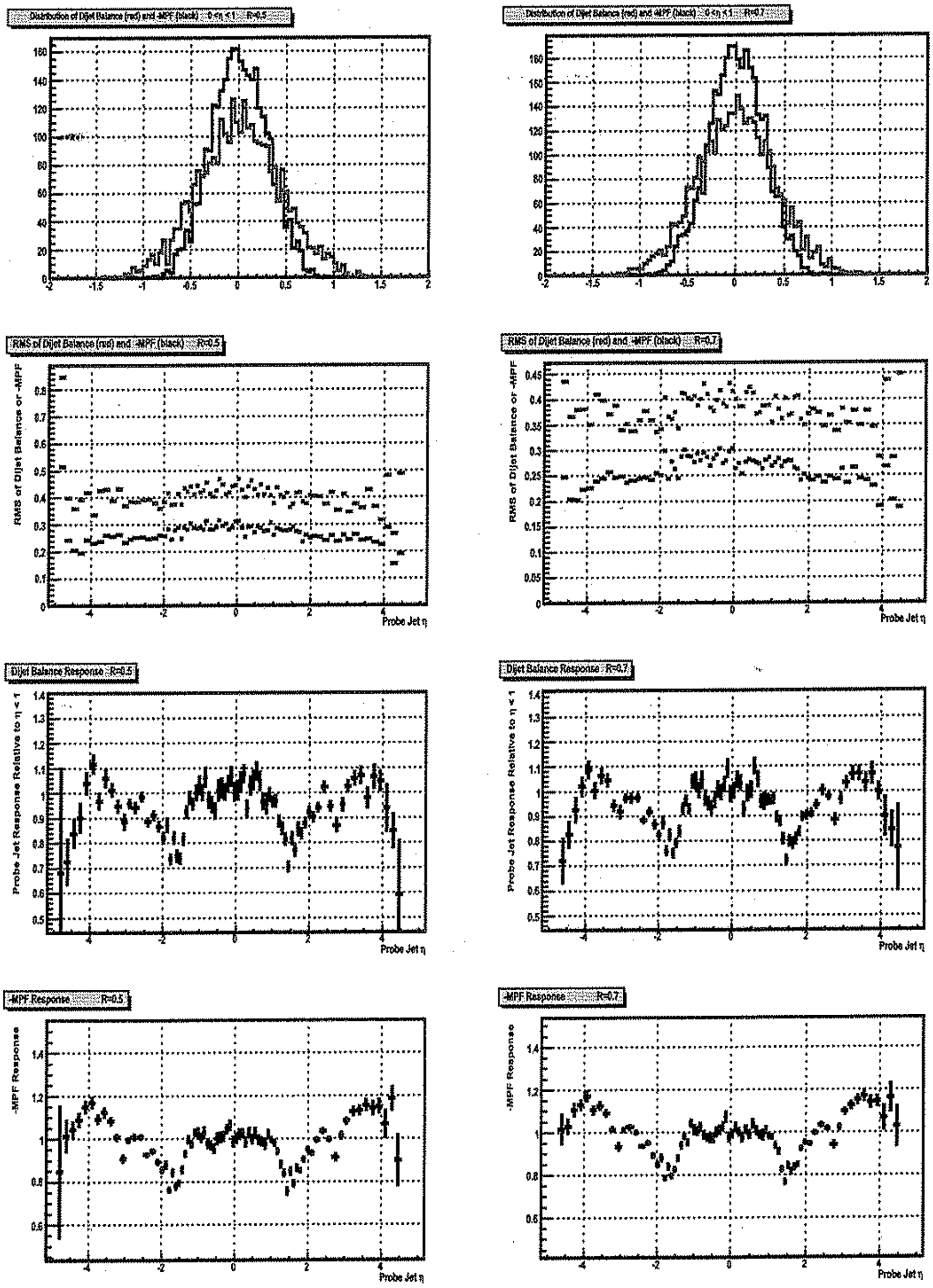

Figure 7.15 Distribution of the $-MPF$ and dijet balance in the detector-η bin of $|\eta| < 1$ (top). RMS of the dijet balance and MPF distribution as a function of detector-η for the $1200 < p_T^{ave} < 1600$ (middle). MPF and dijet balance response in detector-η bins (bottom). Cone size $R = 0.5$ (left plots). Cone size $R = 0.7$ (right plots).

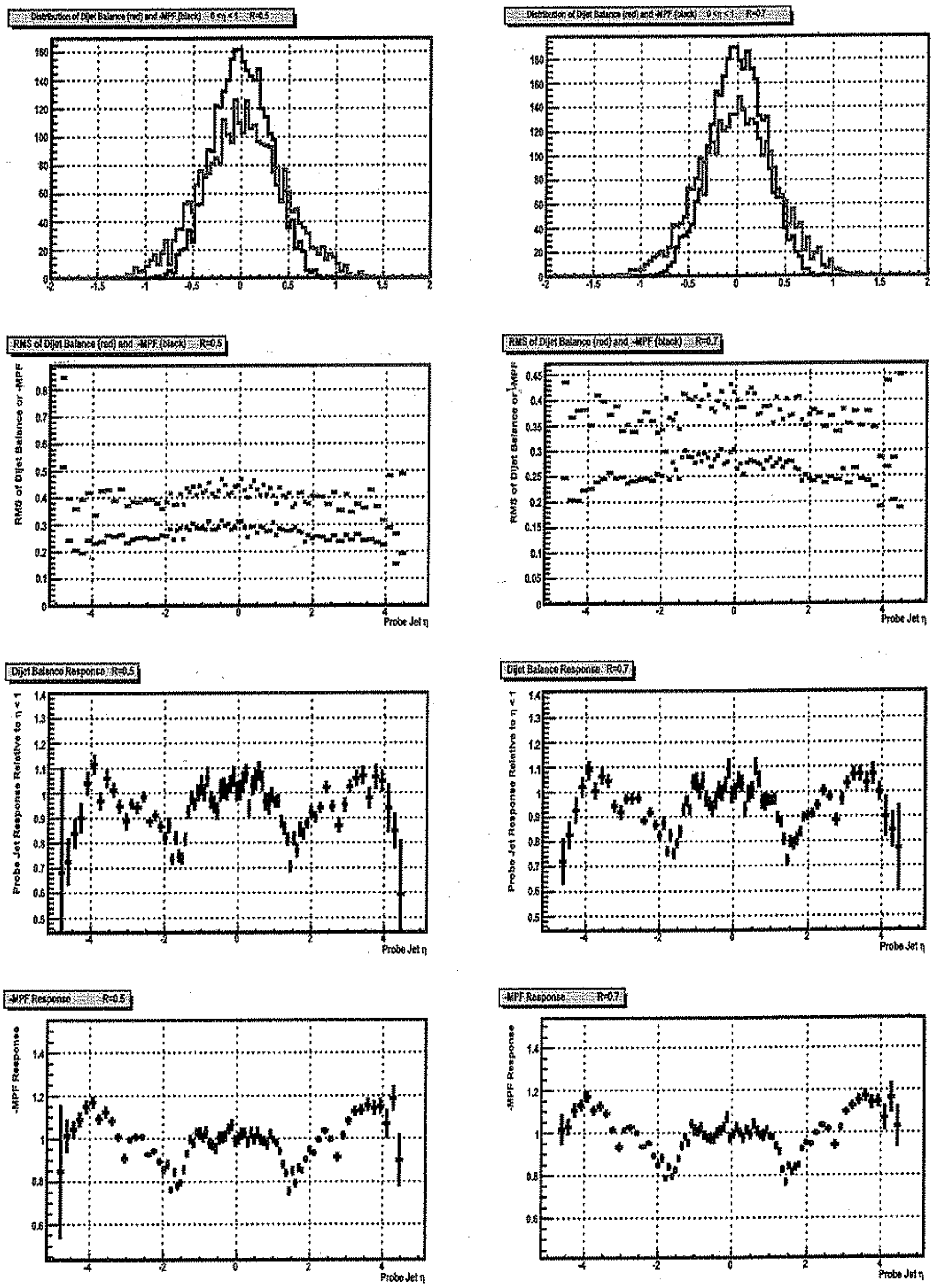

Figure 7.16 Distribution of the $-MPF$ and dijet balance in the detector-η bin of $|\eta| < 1$ (top). RMS of the dijet balance and MPF distribution as a function of detector-η for the $1600 < p_T^{ave} < 2000$ (middle). MPF and dijet balance response in detector-η bins (bottom). Cone size $R = 0.5$ (left plots). Cone size $R = 0.7$ (right plots).

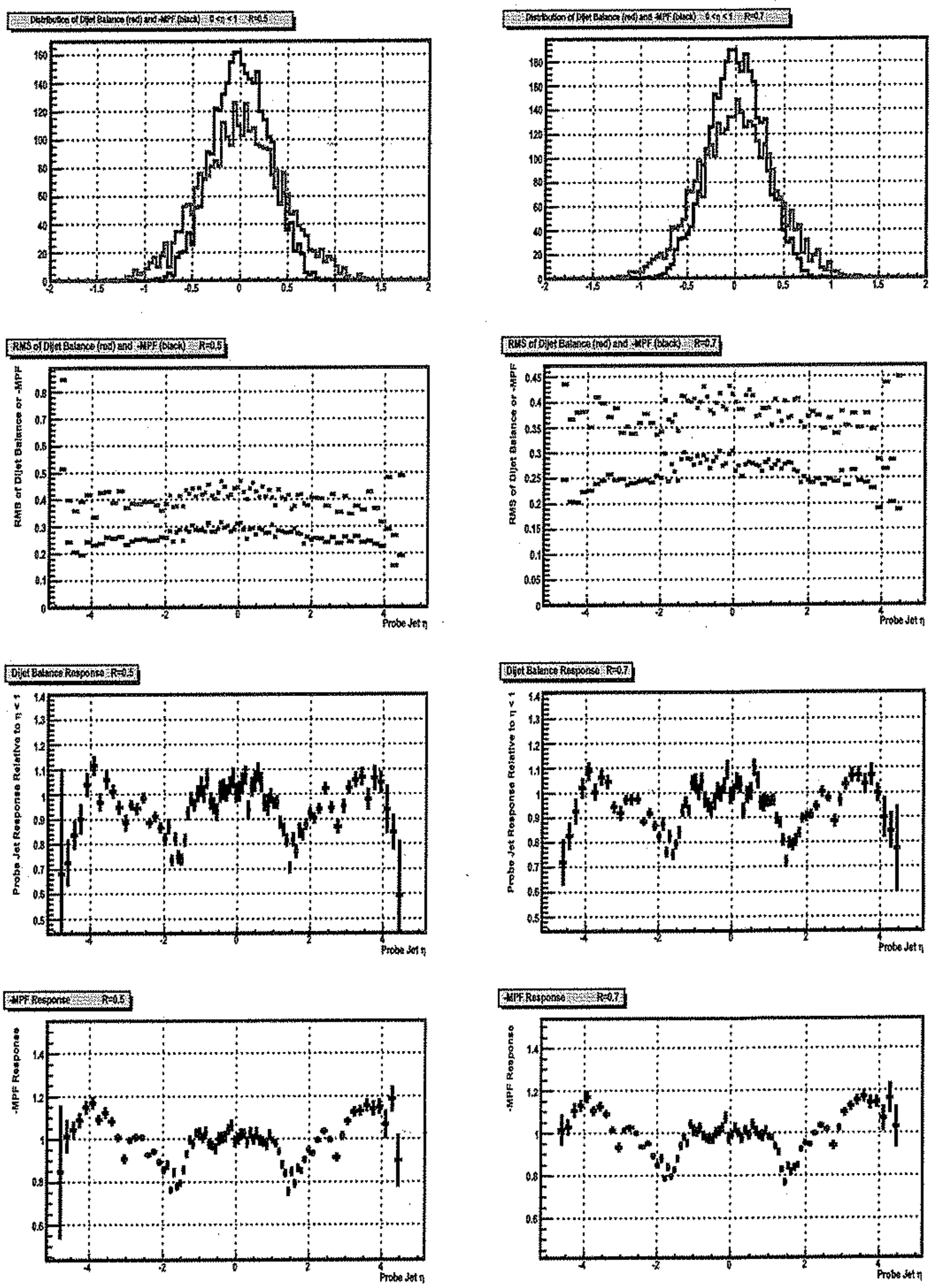

Figure 7.17 Distribution of the $-MPF$ and dijet balance in the detector-η bin of $|\eta| < 1$ (top). RMS of the dijet balance and MPF distribution as a function of detector-η for the $2000 < p_T^{ave} < 2400$ (middle). MPF and dijet balance response in detector-η bins (bottom). Cone size $R = 0.5$ (left plots). Cone size $R = 0.7$ (right plots).

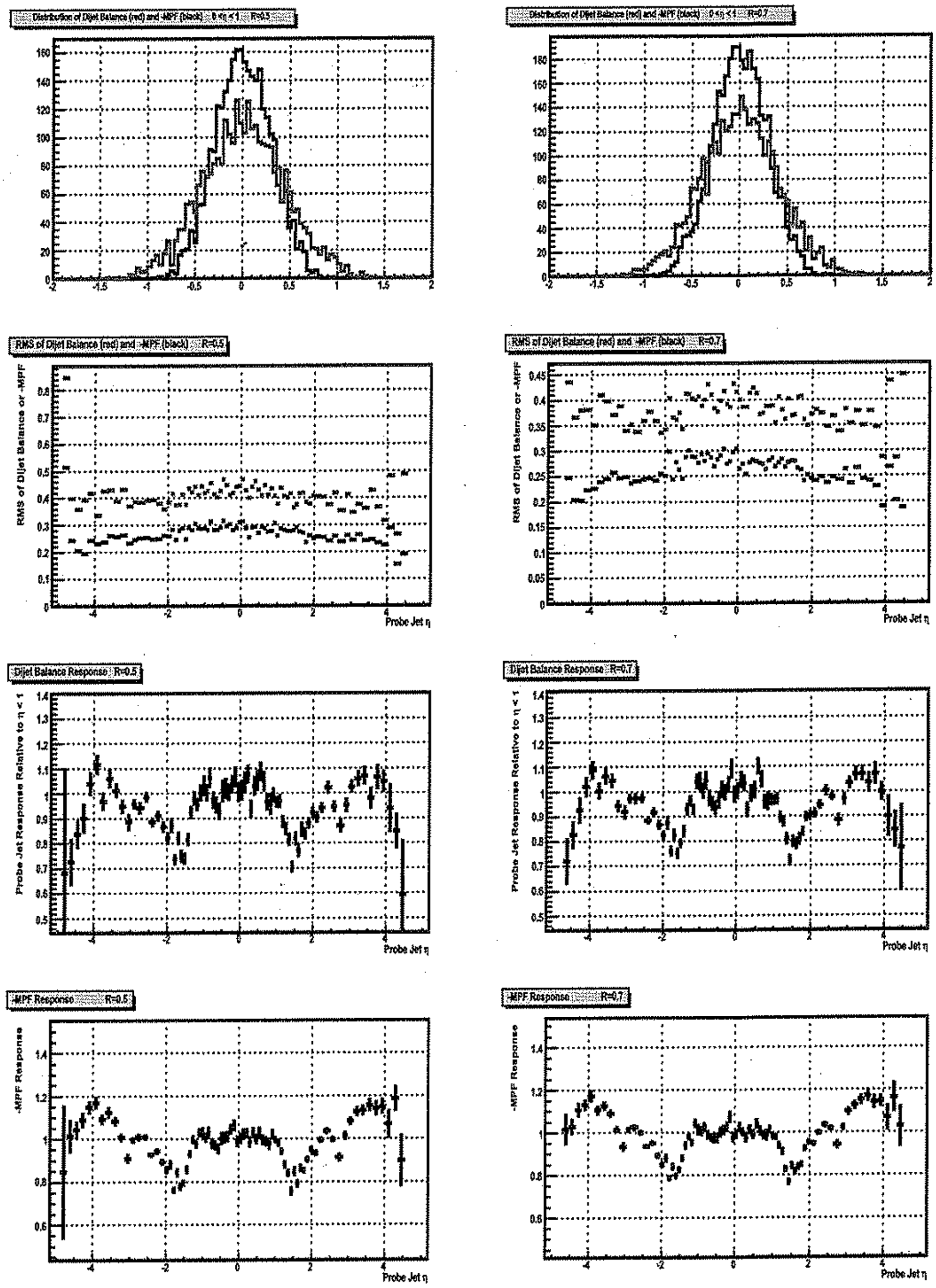

Figure 7.18 Distribution of the $-MPF$ and dijet balance in the detector-η bin of $|\eta| < 1$ (top). RMS of the dijet balance and MPF distribution as a function of detector-η for the $2400 < p_T^{ave} < 2700$ (middle). MPF and dijet balance response in detector-η bins (bottom). Cone size $R = 0.5$ (left plots). Cone size $R = 0.7$ (right plots).

7.2 Comparison of the Dijet Balance and Photon-Jet Balance

In this section, comparisons between the relative jet energy corrections from the dijet balance and photon jet balance methods are presented. Details of the two methods are described in section 6.

7.2.1 Shape of the Dijet Balance and Photonjet Balance Distribution

Figures 7.19 show photon-jet and dijet balance distributions for all of the detector-η bins for the photon-jet and CSA06 data (cone size $R = 0.5$). In all of the detector-η bins, Photon-jet balance distributions are narrower than dijet balance distributions.Also photon-jet distributions are more left side than dijet balance distributions because of using particle level photons were used. Fig. 7.20 shows the larger version of one of the plots in figure 7.19 and the RMS of the photon-jet and dijet balance distributions as a function of detector-η. The RMS of the photonjet balance smaller than that of the dijet balance distribution by roughly 50% for the cone size of $R = 0.5$.

7.2.2 Shape of Response from Dijet Balance and Photonjet Balance

Fig. 7.21 shows response from the photon-jet and dijet balance distributions as a function of detector-η. Shapes of these two plots are very similar.

7.2.3 For Different Cone Sizes

Figures 7.22 is the same as figures 7.20 and 7.21 but for the cone size of $R = 0.7$. In both cases, the RMS of the photon-jet distributions is again smaller than that of the dijet distributions. The difference in the RMS is about 18% for the cone size $R = 0.7$. This can be explained by the fact that the smaller cone size is more sensitive to the soft gluon radiation.

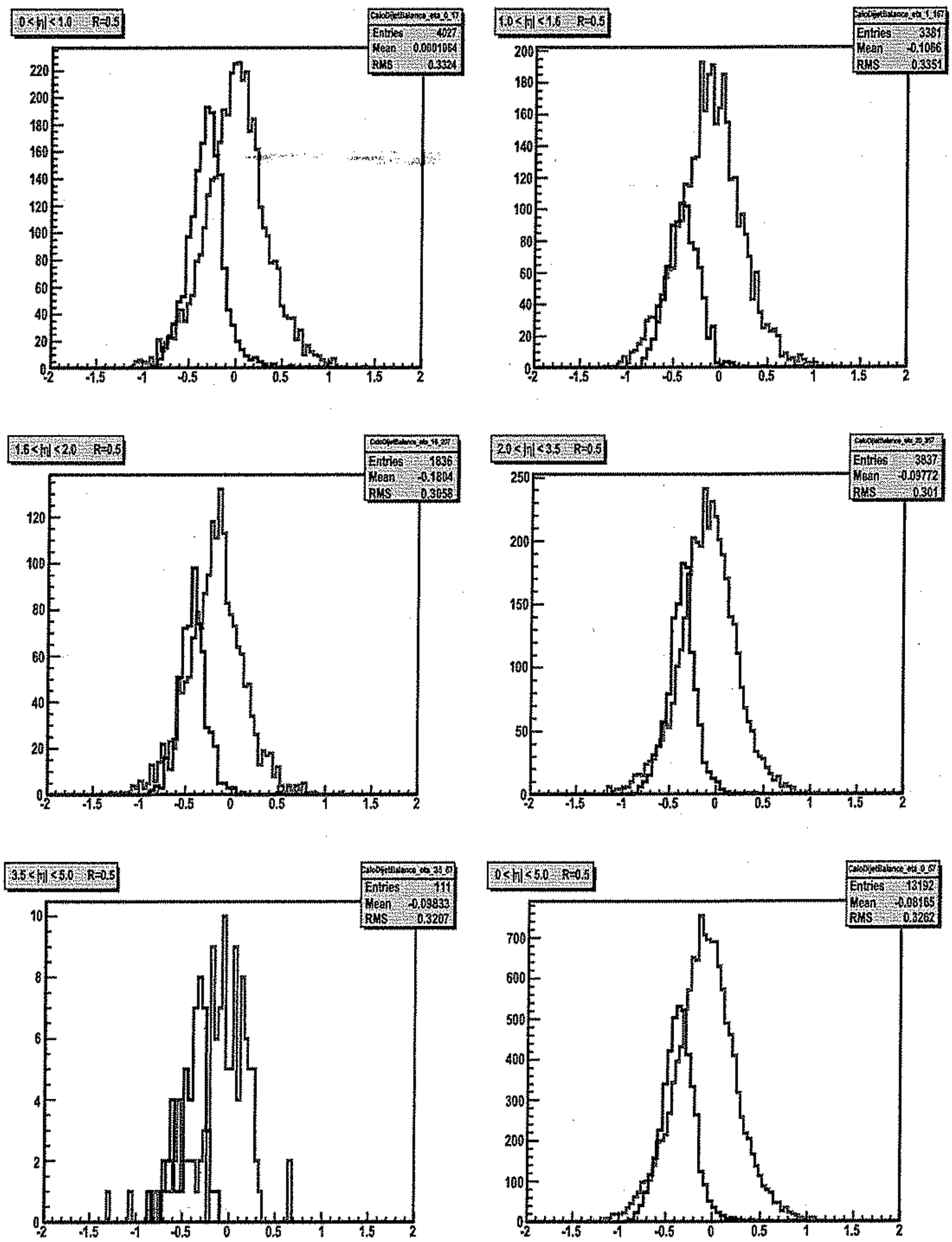

Figure 7.19 Distribution of dijet balance (red) and photon-jet balance (black) for all detector-η bins and cone size $R = 0.5$.

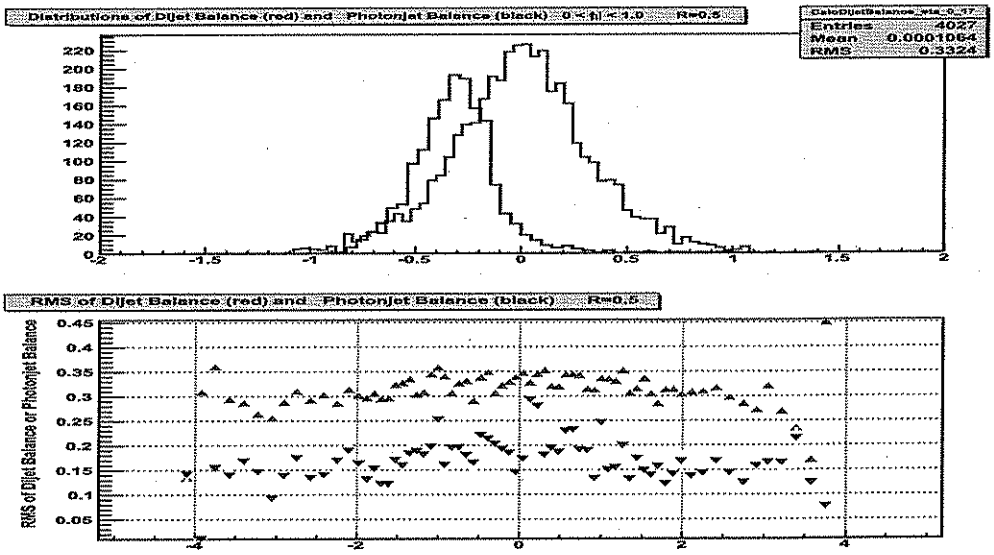

Figure 7.20 Distribution of photon-jet and dijet balance in detector-η bin of $|\eta| < 1.0$ (top). RMS of the photon-jet and dijet balance distributions as a function of detector-η (bottom). For two plots cone size $R = 0.5$.

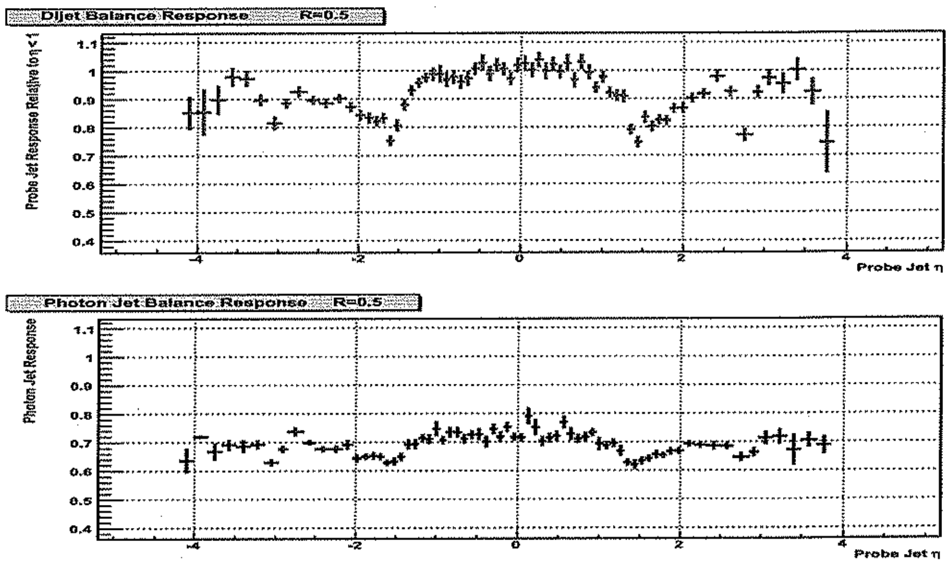

Figure 7.21 Dijet balance response in detector-η bins (top). Photon-jet response in detector-η bins (bottom). For two plots cone size $R = 0.5$.

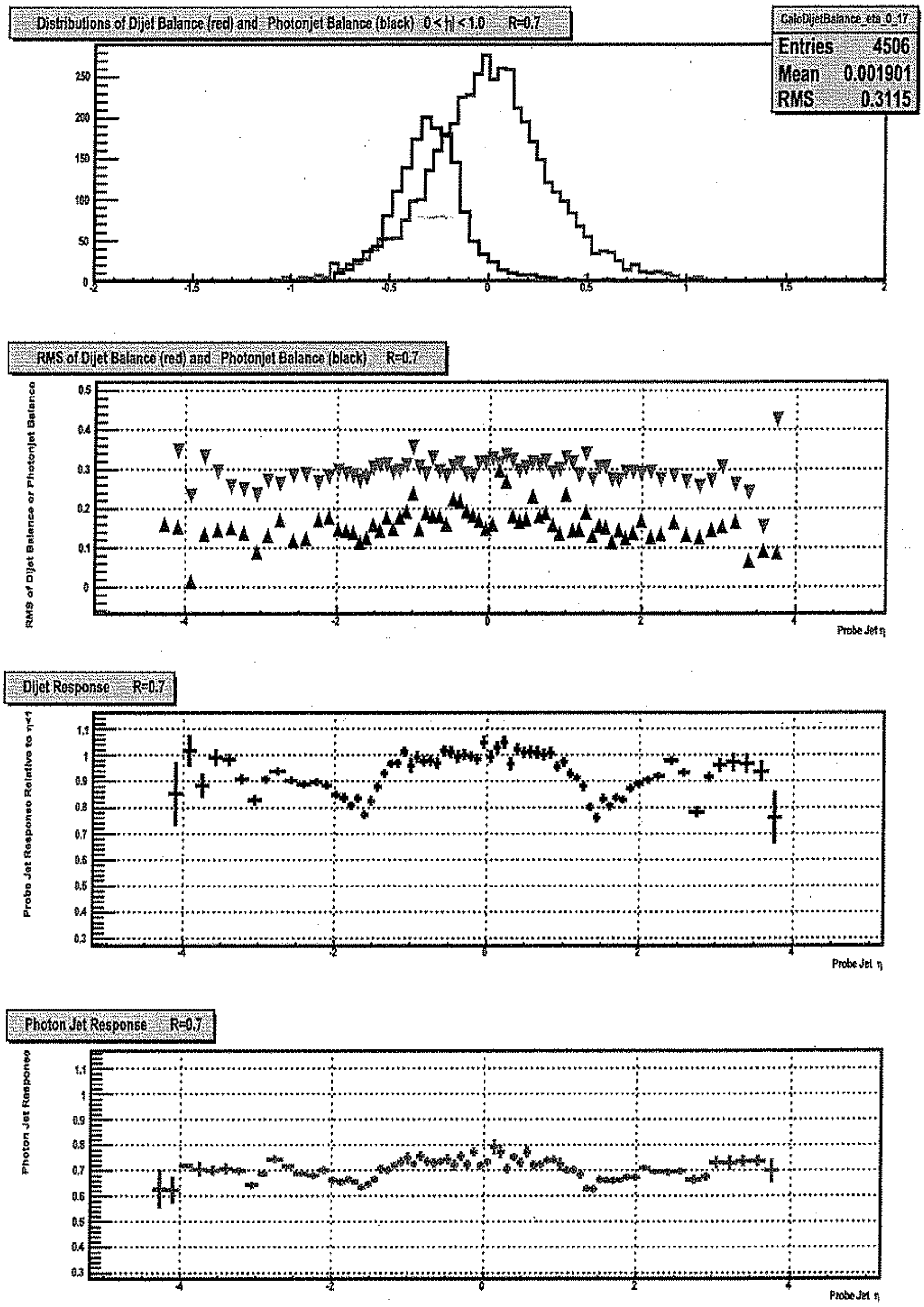

Figure 7.22 Distribution of photon-jet and dijet balance in detector-η bin of $0 < \eta < 1.0$ (top). RMS of the photonjet and dijet balance distributions as a function of detector-η (middle). Dijet balance and photon-jet response in detector-η bins (bottom). All plots were made using cone size $R = 0.7$.

8. CONCLUSION

In this thesis, the relative jet energy correction from the MPF, Dijet Balance and Photon jet Balance methods are compared. Dijet Balancing of reconstructed jets in the CMS data can be used to understand jets without relying on Monte Carlo truth information. Dijet balancing can be used to measure jet response relative to the barrel as a function of η. Dijet balancing can also be used to measure jet resolution. Comparison of dijet balance in the data and the Monte Carlo can then be used to set systematic uncertainties on jet reconstruction.

Here we have performed a first rough demonstration of the technique in order to introduce it to the collaboration. We expect that future work will improve greatly these results.

REFERENCES

HARRIS R., 2005 Jet Calibration from Dijet Balancing. CMS NOTE-2005/034

BHATTI A.A., HATAKEYAMA K., Relative Jet Energy Corrections Using Missing ET Projection Fraction and Dijet Balancing CDF/ANAL/JET/CDFR/6854

CMS Physics Technical Design Report Volume II Physics Performence CERN LHCC 2006-021

CMS Physics Technical Design Report Volume I Detector Performance and Software CERN LHCC 2006-001

http://cmsdoc.cern.ch/cms.html

http://twiki.cern.ch

CURRICULUM VITAE

Name Surname: Mehmet Vergili

Date of Birth: 05.03.1977

Place of Birth: Adana

Nationality: Turkish

Gender: Male

Marrital Status: Single

Contact: vergili@cern.ch

Education:

M.S, Physics Cukurova University, Adana, 2006

Dissertation: Jet Energy Calibration Studies

B.S, Physics, Cukurova University, Adana, Turkey